

INITIAL IONIZATION RATES IN SHOCK-HEATED
ARGON, KRYPTON, AND XENON

Thesis by
Kenneth Edwin Harwell

In Partial Fulfillment of the Requirements
For the Degree of
Doctor of Philosophy

California Institute of Technology
Pasadena, California

1963

ACKNOWLEDGEMENTS

The author wishes to express his sincere appreciation to Professor Robert C. Jahn, who suggested this problem and under whose direction the research was initially carried out. He also wishes to thank Professor Frank E. Marble for his continued support of the research and Professor Hans W. Liepmann for his fruitful discussions of the experimental results.

The assistance of Mr. A. J. Kelly for part of the experimental program is gratefully acknowledged. The help of Mr. F. T. Linton in preparing the figures is also thankfully acknowledged.

The experimental research was carried out with the financial assistance of the Guggenheim Jet Propulsion Center and the Air Force Office of Scientific Research under contract AF 49 (638)-758.

ABSTRACT

The rates of ionization behind strong shock waves in argon, krypton, and xenon are observed by a transverse microwave probe over a range of electron densities low enough that atom-atom inelastic collisions are the rate determining mechanism. Shocks of Mach number 7.0 to 10.0 propagate down a 5 cm square aluminum shock tube into ambient gases at pressures of 3 to 17 mm Hg, heating them abruptly to atomic temperatures of 5500°K to 9600°K . The subsequent relaxation toward ionization equilibrium is examined in its early stages by the reflection, transmission, and phase shifts of a 24.0 Kmc (1.25 cm) transverse microwave beam propagating between two rectangular horns abreast a glass test section. The data yield effective activation energies of 11.9 ± 0.5 ev for argon, 10.4 ± 0.5 ev for krypton, and 8.6 ± 0.6 ev for xenon. These coincide, within experimental error, with the first excitation potentials, rather than the ionization potentials of the gases, indicating that in this range, ionization proceeds via a two-step process involving the first excited electronic state. Within experimental error, the pressure dependence is found to be proportional to the number density squared.

SUMMARY

The purpose of the experiment reported here was to study the low-level ionization of shock-heated noble gases in order to infer whether the reaction mechanism involved is the single atom-atom collisional process or a two-step atom-atom collisional process. The theoretical formulation of the single step process results in the following expression for the rate of ionization,

$$\dot{n} = 4C_a N^2 (kT)^{3/2} (\pi M)^{-1/2} [E_a/2kT + 1] \exp[-E_a/kT]$$

where C_a is the constant initial slope defined by the ionization cross-section, $C_a = C_a(E - E_a)$, E_a is the ionization potential, E is the relative energy of the two colliding atoms, and N , M , and T are the atomic particle density, mass and temperature respectively.

A similar expression results for each of the steps in the two-step process except that the energy E_a becomes the excitation potential for the first step and the difference between the ionization potential and the excitation potential for the second step. Also, the slope constant C_a becomes the one relevant for the first or second step. It can be shown for the temperatures and pressures of this experiment that the first step should be rate controlling after a short initiation period to reach the steady-state concentration of the first excited state population, so that the effective activation energy for the two-step ionization process should be the first excitation potential.

By measuring the ionization rates of the various noble gases as a function of their translational temperatures, the effective activation energy of the atom-atom ionization phase can be determined. Knowing the relevant activation energy, the distinction between the one-step and the two-step ionization routes as the dominant process can be made.

In order to study the atom-atom collisional regime, it was necessary to insure that all electron-atom collisional processes and all impurity reactions were insignificant. Calculations show that the electron-atom rate of ionization becomes comparable to the atom-atom rate at a level of ionization of approximately 10^{-5} . It was found empirically in the course of the experiments described here that impurity levels above about one part per million significantly affected the results. The experiment therefore provided a sample of very pure gas (impurity level of the order of one part in 10^7) of nearly constant temperature in which the ionization proceeded at a level below 10^{-5} for a sufficiently long period of time so that the ionization rates could be precisely determined. Shock waves of Mach number 7 to 10 propagating into monatomic gases at a few mm Hg ambient pressure in a shock tube provided a few hundred microseconds of nearly isothermal flow at electron densities below 10^{13} cm^{-3} .

Using a 24 Kmc(K band) microwave probe, the transmitted power, reflected power, and the transmission phase were measured as a function of time after passage of the shock front. These measurements were corrected for crystal detector nonlinearities,

for deviations from the plane wave-plane slab model caused by refraction of the horn radiation pattern, and for shock attenuation, to arrive at the true electron density growth as a function of time.

The electron density growth $n(t)$ after passage of the shock wave for all three gases was found to be linear from the earliest measurable times indicating that the atom-atom process is the dominant process for the temperature range between 5500°K and 9600°K . Absolute rates of ionization were found to be very slow so that the time required to reach the electron-atom ionization phase varied from 60 microseconds at the highest temperatures to 100 milliseconds at the lowest temperatures.

Using the slopes of Arrhenius plots of $\ln \dot{n}$ versus $1/kT$, the activation energy E_a was determined for each of the three gases. The experimentally determined values of 11.9 ± 0.5 ev for argon, 10.4 ± 0.5 ev for krypton, and 8.6 ± 0.6 ev for xenon are in close agreement with the first excitation potentials of 11.55 ev for argon, 9.92 ev for krypton, and 8.32 ev for xenon, indicating that the two-step mechanism is the dominant process for ionization at the temperatures considered.

The pressure sensitivity of the ionization reaction is so mild compared with the exponential temperature dependence that the pressure dependence tended to be obscured by random fluctuations introduced into the data by slight variations in impurity levels and by slight uncertainties in the thermal history behind the shock wave. Within experimental limitations, the rate of ionization was found to be proportional to the pressure squared. This is a further indication that the atom-atom process is the mechanism for ionization at the

pressures of 3 to 17 mm Hg and temperatures of 5500°K to 9600°K experienced in this experiment.

The results quoted above were derived from the purest ambient gases obtainable using a high purity shock tube that had a leak rate of less than 5×10^{-4} microns/min. and an outgassing rate of about 2×10^{-2} microns/min. To reduce the level of impurities introduced by the outgassing of the shock tube, the test gas was allowed to flow continuously down the entire length of the shock tube at rates as high as 1000 times the outgassing. The ultimate impurity level prevailing in the gas at the time of passage of the shock front was reducible by this technique to about one part in 10^7 . During the course of the experiments the flow system underwent several modifications to obtain these purities when preliminary data gave results depending on the specific impurity levels. It was found that impurity levels above one part per million significantly biased the results and that impurity levels above ten parts per million completely obscured the reactions of interest.

TABLE OF CONTENTS

<u>PART</u>	<u>TITLE</u>	<u>PAGE</u>
	ACKNOWLEDGEMENTS	ii
	ABSTRACT	iii
	SUMMARY	iv
I.	INTRODUCTION	1
II.	PHYSICAL FOUNDATIONS OF THE EXPERIMENT	3
	1. Ionization by Atom-Atom Collisions	4
	2. Ionization by Electron-Atom Collisions	8
	3. Break-Even Point Between Atom-Atom and Electron-Atom Ionization Processes	9
III.	APPARATUS	10
IV.	APPLICATION OF MICROWAVES TO THE DETERMINATION OF ELECTRON DENSITY AND THE REDUCTION OF EXPERIMENTAL DATA	12
	1. Interaction of Microwaves with Plasma	12
	2. Design of the Microwave Probe	16
	3. Interpretation of Experimental Data	20
V.	SHOCK ATTENUATION	27
VI.	RESULTS	32
	1. Argon	32
	2. Krypton	36
	3. Xenon	38
VII.	CONCLUSIONS	40
	REFERENCES	42
	FIGURES	44

I. INTRODUCTION

The ionization of monatomic gases has been studied for many years by using the most successful electron-beam technique. Using this method, Ramsauer⁽¹⁾ was perhaps the first to obtain quantitative absolute measurements of the total cross-sections in the noble gases as a function of electron velocity. He observed the now famous Ramsauer effect of a pronounced maximum in the cross-sections for argon, krypton, and xenon for electrons with energies in the neighborhood of 8 to 15 ev. He also found that the gases are practically transparent to electrons of about one electron volt energy. This transparency of the heavier noble gases for electron energies of one ev was also discovered by Townsend and Bailey⁽²⁾ and is sometimes called the Ramsauer-Townsend Effect. In the range of electron energies 0.5 to 100 ev, the cross-sections for electron-atom collisions were studied by several investigators^(3, 4, 5) over the next few years after Ramsauer's work. As a result, very precise quantitative information is available for electron-atom collisions. For specific details on the electron-atom collisions and information concerning other experiments, refer to Massey and Burhop⁽⁶⁾.

Largely because the experimental study of collisions in which both of the colliding systems are of atomic mass is very difficult, the existing data for atom-atom collisions is not as extensive as in the electron-atom case. There are many problems inherent in this technique, but the two major problems have to do with the production of a beam of gas atoms of precisely known composition and energy and the measurement of the strength of the beam at any point.

Several experiments have been attempted using atomic beams⁽⁶⁾, but virtually no precise data using this technique exists for low energies.

One method of generating a body of hot gas of reasonably well known gas dynamical properties is the shock tube technique. Shock waves have been used successfully to generate gas with temperatures in the low energy range. Petschek and Byron⁽⁷⁾ have considered the approach to equilibrium ionization behind shock waves in argon. They found that the mechanism for approaching equilibrium consists of two stages. The second stage, where the degree of ionization is sufficiently large, was found to consist of electron-atom collisions for gas temperatures in the range of $10,000^{\circ}$ to $30,000^{\circ}$ K. The rates of ionization by electron-atom collisions were calculated and found to be in agreement with their experimental measurements. They also concluded that the first stage of ionization, which must account for the initial production of electrons, must be due to an atom-atom collisional process that is significantly affected by the presence of small traces of impurities.

Weymann⁽⁸⁾ has considered the mechanisms for thermal ionization and has postulated a two-step process for the initial stage of ionization in which an atom is raised to the first excited electronic state by a collision with another atom and is then ionized by a second collision with an atom. He states that it is not necessary to postulate that impurities influence the ionization rate of the noble gases as long as the impurity concentration is below about 10^{-3} .

Sturtevant⁽⁹⁾ has considered the ionization of argon for temperatures in the range 8500 to 11,000°K and pressures 60 to 100 microns by measuring the effusive electrical current through a small orifice in the end wall of a shock tube and has found that the ionization of argon results from a complicated series of consecutive reactions. He found that the initiation process is very slow and therefore has a strong effect on the relaxation time.

The primary purpose of the experiment reported here is to infer the reaction mechanisms involved in the early stages of ionization from measurements of the ionization rates. The ionization rates of noble gases in a shock tube are determined experimentally by examining the buildup of ionization density behind the shock front by means of a microwave technique.

II. PHYSICAL FOUNDATIONS OF THE EXPERIMENT

The purpose of the experiment reported here is to study the low-level ionization of shock-heated argon, krypton, and xenon. "Low-level" ionization is defined to be a degree of ionization sufficiently small that the relatively efficient electron-atom collisional processes are so rare that the gas must have recourse to the much less effective heavy particle collisions to generate the first few ions.

A variety of reaction schemes can be proposed for this low-level ionization, including not only the "pure gas" reactions,

(a) Ionization by a single atom-atom collision:



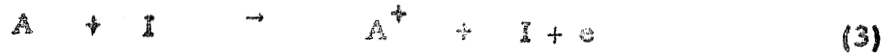
and

(b) Ionization by successive atom-atom collisions⁽⁸⁾:



but also, because of the relatively high atomic levels and small collision cross-sections of the above pure gas reactions the "impurity" reactions,

(c) Direct:



where the impurity particle, I, may be in the gas or on the wall of the container, or

(d) Catalytic, by means of charge exchange:



The theoretical formulation of any of these reactions is quite similar and is considered in the next section.

1. Ionization by Atom-Atom Collisions

Assuming that the gas atoms are in Maxwellian equilibrium defined by,

$$dN = N(\vec{v})d\vec{v} = N \left(\frac{M}{2\pi kT} \right)^{3/2} \exp \left[-\frac{M|\vec{v}|^2}{2kT} \right] d\vec{v} \quad (5)$$

where N , M , T and \vec{v} are the atomic particle density, mass, temperature, and velocity, the frequency with which process (a) proceeds in the gas may be written⁽¹⁰⁾:

$$\begin{aligned}
 v_a &= N^2 \iint \Omega_a(g) g f(\vec{v}_j) f(\vec{v}_k) d\vec{v}_j d\vec{v}_k \\
 &= N^2 \frac{1}{2} \left(\frac{M}{2\pi kT} \right)^3 \iint e^{-\frac{M}{2kT} [|\vec{v}_j|^2 + |\vec{v}_k|^2]} \Omega_a(g) g d\vec{v}_j d\vec{v}_k. \quad (6)
 \end{aligned}$$

$g = |\vec{v}_j - \vec{v}_k|$ is the relative speed between the colliding atoms j and k , and $\Omega_a(g)$ is the ionization cross section. In terms of the velocity of the center of mass of the two colliding atoms, $\vec{v}_0 = (\vec{v}_j + \vec{v}_k)/2$,

Eqn. (6) may be rewritten as

$$v_a = \frac{1}{2} N^2 \left(\frac{M}{2\pi kT} \right)^3 \int_0^{\infty} e^{-Mv_0^2/kT} 4\pi v_0^2 dv_0 \int_{g_0}^{\infty} e^{-Mg^2/4kT} \Omega_a(g) 4\pi g^3 dg. \quad (7)$$

Since the ionization cross-section $\Omega_a(g)$ is identically zero for energies transferred that are less than a certain threshold energy E_a , g_0 is defined as the minimum relative speed for process (a) to occur and is related to E_a in the following way:

$$g_0 = (4E_a/M)^{\frac{1}{2}}. \quad (8)$$

The magnitude of v_a relies on the dependence of the ionization cross-section, Ω_a , on the relative particle speed at impact.

Weymann⁽⁸⁾ assumes Ω_a is constant from g_0 to ∞ and obtains:

$$v_a = 2N^2 \Omega_a \left(\frac{kT}{\pi M} \right)^{\frac{1}{2}} \left[\frac{E_a}{kT} + 1 \right] \exp\left(-\frac{E_a}{kT}\right). \quad (9)$$

However, most inelastic collision cross-sections have energy dependences rising steeply from threshold. Since we will be concerned with a situation where $kT \ll E_a$, it seems more reasonable to approximate Ω_a by a linear dependence on energy

(transferred) above threshold:

$$Q_a = C (E - E_a) = \frac{1}{4} M C_a (g^2 - g_0^2) . \quad (10)$$

Using this form of energy dependence for the cross-section, the collision frequency becomes:

$$\nu_a = 4C_a N^2 (kT)^{3/2} (\pi M)^{-1/2} \left[\frac{E_a}{2kT} + 1 \right] \exp(-E_a/kT) . \quad (11)$$

Taking the natural logarithm and differentiating with respect to $1/kT$,

$$\frac{d(\ln \nu_a)}{d(1/kT)} = -E_a \left[1 + \frac{3kT}{2E_a} - \frac{1}{\frac{E_a}{kT} + 2} \right] . \quad (12)$$

For $kT \ll E_a$,

$$\frac{d(\ln \nu_a)}{d(1/kT)} \approx -E_a . \quad (13)$$

This expresses the familiar result that the slope of an Arrhenius plot of the logarithm of the rate of ionization versus $1/kT$ is approximately the activation energy for the process being considered.

An identical result prevails for the first step of reaction (b), except that the threshold energy is now the first excitation potential, E_b , and the cross-section involved is that for excitation to the first excited state, A^* :

$$Q_b = C_b (E - E_b) . \quad (14)$$

whether the excitation rate, ν_b , computed in this manner represents the composite rate of the two-step ionization process depends on the relative efficiency of the second step — the ionization from the excited state. This in turn depends on the effective lifetime of A^* , relative to the effective inelastic collision frequency for this process. Since in the noble gases the energy increment involved in the second step,

$E_a = E_p$, is much less than that for the first step, E_p , since the geometrical "size" of an excited gas atom presumably exceeds that of its ground state, and since a continuum of final states is available for the second step compared to a discrete level for the first, it is reasonable to anticipate significantly higher collision efficiencies for the second step. The issue then depends on the level of "steady-state" concentration of A^* which can be sustained, i. e., on its effective lifetime. Weymann⁽⁸⁾ states that the individual lifetime against radiative decay ($\sim 10^{-8}$ sec.) is effectively extended by several orders of magnitude by a trapping of the resonance radiation emitted upon such decay. That is, a photon emitted upon decay of one excited atom is absorbed in the excitation of an adjacent atom, subsequently re-emitted by that atom, re-absorbed nearby, etc., over many such cycles before escaping from the body of the gas. If his estimates are correct, for particle densities above 10^{15} cm^{-3} , the first step should be rate-controlling (after a short induction period to reach steady-state A^* population), and the effective activation energy for the two-step ionization process should be E_p , the first excitation potential.

The primary purpose of this experiment is to determine the effective activation energy of atom-atom ionization of various noble gases, by measuring their ionization rates in this regime as a function of their translational temperature, and thereby to distinguish between the one-step and two-step ionization routes (a) and (b). To accomplish this purpose, it clearly is necessary to insure that the impurity reactions, (c), and all electron-atom inelastic collisions are rendered insignificant. Impurity reactions

are well known to be troublesome in such studies⁽⁷⁾, as could be anticipated from the comparatively low excitation and ionization potentials of many metal and molecular vapors. It is found empirically in the course of the experiments described here that impurity levels above one part per million significantly bias the results. Impurity levels above ten parts per million completely obscure the reactions of interest.

2. Ionization by Electron-Atom Collisions

The suppression of electron-atom reactions dictates an upper limit on the ionization density which can be tolerated. An analysis similar to that used for the atom-atom case is used to calculate the ionization rates for electron-atom ionization⁽⁷⁾.

Assuming that the atoms are at rest and the electrons are Maxwellian in their energy,

$$d n(E) = \frac{2m}{\pi^{3/2}} (kT_e)^{-3/2} E^{1/2} \exp(-E/kT_e) dE \quad (15)$$

where T_e is the electron temperature and n is the electron density, then the rate of ionization is given by:

$$v_e = N \int_{E_e}^{\infty} Q(E) v n(E) dE = (2/m)^{1/2} N \int_{E_e}^{\infty} E^{1/2} Q(E) n(E) dE. \quad (16)$$

Again making the assumption of a linear rise of the cross-section with increasing energy above a threshold energy, E_e :

$$Q(E) = C_e (E - E_e) \quad (17)$$

the rate of ionization is given by

$$v_e = 4(2/\pi m)^{\frac{1}{2}} C_e N_a (kT_e)^{3/2} [E_e/2kT_e + 1] \exp(-E_e/kT_e) \quad (18)$$

3. Break-Even Point Between Atom-Atom and Electron-Atom Ionization Processes

The ratio of ionization rates by atom-atom collisions to that by electron-atom collisions may be expressed for $T_e = T$,

$$\frac{v_a}{v_e} = \left(\frac{m}{2M}\right)^{\frac{1}{2}} \frac{N}{n} \frac{C_a}{C_e} \quad (19)$$

or the corresponding expression involving v_b and C_b . The coefficients C_a and C_b are very poorly known. Extrapolation of high energy data from Massey and Burhop⁽⁶⁾ and von Engel⁽¹¹⁾, suggest values of approximately 10^{-19} cm²/ev. Petschek and Byron⁽⁷⁾ quote values for C_e of 7×10^{-18} cm²/ev for excitation and 2×10^{-17} cm²/ev for ionization. The guess is then that

$$\frac{C_a}{C_e} \approx \frac{C_b}{C_e} \approx 0.01, \quad (20)$$

a value not inconsistent with the equivalent velocity hypothesis.

On this assumption, the break-even point occurs in argon at

$$\alpha = n/N \approx 2 \times 10^{-5} \quad (21)$$

The desired experiments therefore should provide a sample of very pure gas of constant (translational) temperature in which ionization proceeds at a level below 10^{-5} , at a fast enough rate, yet for a long enough time that the rate can be precisely determined. Shock waves of Mach number range 7 to 10 propagating into monatomic gases at a few mm Hg ambient pressure in a shock tube, provide a

few hundred microseconds of nearly isothermal flow at total densities of approximately 10^{18} cm^{-3} . A diagnostic device sensitive to free electron densities below 10^{13} cm^{-3} is thus required, with adequate spatial and temporal resolution to follow the axial gradients established by the prevailing ionization reaction rate in this zone of gas. The choice was a 1.25 cm wavelength transverse microwave probe which will be described later.

III. APPARATUS

Since the purity of the test gas was known in advance to be a critical factor in such experiments⁽⁷⁾, the shock tube employed was specifically designed to combine the necessary ruggedness for high shock strength operation with a reasonable level of cleanliness. The major portion of the tube was assembled from lengths of cold extruded, heavy-wall aluminum pipe (6063 - T5), having an interior cross-section 2 inch square, with 5/32 inch flat corner fillets and a 3/4 inch wall thickness⁽¹²⁾. A rectangular channel was thus provided without longitudinal seams. The lengths of tubing were joined with simple "O-ring" butt joints, constrained by split-ring flanges⁽¹³⁾. Access ports to the tube were restricted to a minimum number and all were covered with cylindrical "O-ring" flange fittings.

The test section was a 10 inch length of heavy wall, precision bore, square pyrex pipe whose interior surface, hot-formed over a stainless steel mandril, precisely matched the interior dimensions of the adjacent aluminum sections of the shock tube. This pyrex section was attached to the tube, 20 feet from the diaphragm, by means of a heavy steel yoke which permitted precise alignment of the inner walls at the junctions with the aluminum sections. Two

feet beyond the test section, the tube terminated into a 10 cubic foot stainless steel dump tank, needed to reduce the final pressure in the tube to a level tolerable to the glass pipe.

The desired shock strengths were generated by pressure bursting diagonally-scribed aluminum and copper diaphragms of various thicknesses by various types and pressures of driver gas. Hydrogen up to 1000 psi was needed to generate the strongest shocks in argon. Helium was used for the weaker shocks in argon, and for all of the strengths generated in krypton. Various helium-argon mixtures were used as drivers for xenon.

Thin platinum film gauges, mounted on small glass plugs, recorded the time of passage of the shock wave over given positions along the tube (refer to Fig. 1). The amplified responses of two film gauges adjacent to the test section, fed into a Berkeley 7260 time interval crystal counter yielded the shock Mach number at the test section to better than one percent. The attenuation of the shock wave during its propagation down the tube was determined by displaying the signals from a series of film gauges directly onto a Tektronix 551 dual beam oscilloscope.

Largely by trial and error, the absolute leak rate of the tube and its associated gas handling equipment was reduced to less than 5×10^{-4} microns/min., which was felt to be adequate in comparison with the outgassing rate of about 2×10^{-2} microns/min. which prevailed even after heating the entire tube to 100°C for several hours. To combat the introduction of impurities via the outgassing, the test gas was allowed to flow continuously down the shock tube from a valve near the mouth of the dump tank (as shown in Fig. 1), to a

valve near the diaphragm, at rates as high as 1000 times the outgassing. These valves remained open until slammed shut by the passage of the shock wave over their ports. The ultimate impurity level prevailing in the gas at the time of passage of the shock front was reducible by this technique to about 1 part in 10^7 .

IV. APPLICATION OF MICROWAVES TO THE DETERMINATION OF ELECTRON DENSITY AND THE REDUCTION OF EXPERIMENTAL DATA

The ionization density of the gas was measured by a transverse microwave probe operating at a frequency of 24Kmc (K band). The microwave probe used in this experiment has been described in detail elsewhere^(14, 15) and will be reviewed only briefly here.

1. Interaction of Microwaves With Plasma

For a uniform medium of finite conductivity, but a net charge density of zero, Maxwell's equations can be manipulated to give a harmonic wave equation for the electric field \vec{E} ,

$$\nabla^2 \vec{E} + k_0^2 \left[1 - i \left(\frac{\sigma}{\epsilon \omega} \right) \right] \vec{E} = 0 \quad (22)$$

where ω is the impressed angular frequency, $k_0 = \omega(\mu_0 \epsilon_0)^{\frac{1}{2}}$ is the vacuum propagation exponent, ϵ is the dielectric permittivity, and σ is the electrical conductivity. Assuming propagation in the z direction, the plane wave solutions are given by

$$\vec{E} = \vec{E}_0 e^{i(\omega t + k^* z)} \quad (23)$$

$$\text{where } k^* = k_0 \left[1 - i \left(\sigma / \epsilon \omega \right) \right]^{\frac{1}{2}} \quad (24)$$

Here we take the point of view that the field induced oscillations of the free electrons are a real current giving rise to a conductivity of the medium. Next, we relate the conductivity of the ionized gas to the average drift velocity of the electrons by means of the two fluid concept where the ion current contribution is neglected.

Solving the equation of motion of an "ensemble-average" electron,

$$m \vec{v}_d + m \nu_c \vec{v}_d = e \vec{E} e^{i\omega t} \quad (25)$$

for the drift velocity, we arrive at the complex conductivity of the medium:

$$\sigma^* = \frac{ne v_d}{|E|} = \frac{ne^2}{m(\nu_c + i\omega)} = \frac{\epsilon \omega_p^2}{\nu_c + i\omega} \quad (26)$$

where $\omega_p = (ne^2/\epsilon m)^{1/2}$ is defined as the electron plasma frequency, n is the free electron number density, and ν_c is the effective collision frequency.

The quantity ν_c is an effective collision frequency for momentum transfer of electrons on heavy particles. The explicit evaluation of ν_c from atom cross-sections has been discussed by Massey and Burhop⁽⁶⁾, Chapman and Cowling⁽¹⁰⁾, and Schultz⁽¹⁶⁾.

ν_c can be estimated from the single particle momentum-transfer (diffusion) cross-sections Ω_d averaged over the appropriate electron distribution function

$$\nu_c = \sum_j N_j \overline{\Omega_{dj} v} \quad (27)$$

where N_j is the number density of the j -th species of heavy particles (molecules or ions). Actually, the effective ν_c may be evaluated from two simultaneous microwave measurements on the gas of interest

and need not be known precisely in advance. A crude calculation was made using the scattering cross-section given by Kivel⁽¹⁷⁾ which gave a value of $\nu_c / \omega = 0.025$. A value of $\nu_c / \omega = 0.03$ was obtained using absorption coefficient data from Normand⁽⁵⁾. These estimates are lower than the average measured values by a factor of two to ten, but are indicative of order of magnitude agreement within the accuracy of the calculated estimates.

Substituting (26) into (24) and separating into real and imaginary parts, the propagation exponent is

$$k^* = k_r - i k_i$$

$$k_r = (k_0/2)^{1/2} \left\{ (1 - F) + [(1 - F)^2 + F^2(\nu_c/\omega)^2]^{1/2} \right\} \quad (28)$$

$$k_i = (k_0/2)^{1/2} \left\{ -(1 - F) + [(1 - F)^2 + F^2(\nu_c/\omega)^2]^{1/2} \right\} \quad (29)$$

where

$$F = (\omega_p/\omega)^2 / [1 + (\nu_c/\omega)^2]$$

Essentially, these two functions, k_r and k_i , completely describe plane wave propagation in an ionized gas of free electron density, n , and effective collision frequency ν_c .

To use these expressions one must consider the particular experimental set-up, which will impose certain boundary conditions that must be satisfied. For example, for the experiment under study here, the plane wave train would have to travel through two air regions, two glass regions, and through the plasma itself, so that there would be four boundary surfaces on which conditions must be satisfied. By making the glass walls half wave plates reduces the problem to the simplest possible geometry⁽¹⁴⁾—that of a plane wave incident normally on a uniform plane slab of ionized gas as shown in Fig. 2. Allowing

positive and negative traveling waves of the form,

$$e^{i(\omega t \pm k^* z)}$$

and satisfying the boundary conditions at the two interfaces which require continuity of the electric and magnetic components of the total wave fields, the following expressions result for the complex reflection and transmission coefficients:

$$\frac{E_r}{E_o} = R e^{i\phi_R} = \frac{(k_o^2 - k^{*2})(e^{ik^*L} - e^{-ik^*L})}{(k_o + k^*)^2 e^{ik^*L} - (k_o - k^*)^2 e^{-ik^*L}} \quad (30)$$

$$\frac{E_t}{E_o} = T e^{i\phi_T} = \frac{4k_o k^* e^{ik_o L}}{(k_o + k^*)^2 e^{ik^*L} - (k_o - k^*)^2 e^{-ik^*L}} \quad (31)$$

where R , T , and ϕ_R , and ϕ_T are real scalars and the notation is that given in Fig. 2. Since most microwave detection devices measure power, T^2 , R^2 , ϕ_R , ϕ_T are the measurable quantities of interest where ϕ_R and ϕ_T are measured by an interference of the reflected or transmitted signal with an undisturbed component, for example:

$$\begin{aligned} P_R &= 1 + R^2 - 2R \cos \phi_R \\ P_T &= 1 + T^2 - 2T \cos \phi_T \end{aligned} \quad (32)$$

Solution of equations (30)-(32) using (28) and (29) were obtained using and IBM 7090 computer⁽¹⁸⁾ and are plotted in Fig. 3 to 6 for a slab of width $L = 4 \lambda_o$ which coincides with L of the experimental set-up.

In the cases shown, for very small ratios of collision frequency to field frequency, ν_c / ω , nearly periodic fluctuations in

R^2 and T^2 occur as the free electron density increases from zero. These arise from interference between the primary and multipass signals, as in a conventional parallel-plate interferometer. As the resonant electron density n_p is approached, the attenuation increases, discriminating against the components which make additional passes through the slab and the interference disappears. These interference bumps also become less pronounced for the larger collision frequencies where serious damping sets in before the surface reflections become significant.

2. Design of the Microwave Probe.

In order for the above analysis to apply to the experimental set-up, the microwave probe must be designed to closely simulate the plane wave-plane slab geometry. The first of these requirements was solved by a pair of specially designed and matched pyramidal horns looking at each other across the test section and suitably matched to the test section walls. The planarity of the radiated wave front is determined by the apex angles of the horn. The amount of longitudinal component in the wave train's magnetic vector depends on the ratio of the width of the horn mouth in the \vec{H} plane to the wavelength⁽¹⁹⁾. The focusing and collimation of the radiated field in the near and intermediate field regions where one must normally operate is a complex function of both horn mouth dimensions⁽²⁰⁾. The horn dimensions selected must therefore be a compromise which best optimizes the field pattern for the particular application of interest. For our particular case where the ionization patterns are essentially one dimensional in the flow direction, the extent of the field in the direction parallel to the

gas flow must be minimized while maintaining good field uniformity in the transverse directions. A series of graphical studies, some empirical data from earlier experiments, and certain near-field antenna calculations⁽²⁰⁾ were used to arrive at the horn dimensions shown in Fig. 7. The wave fronts radiated by these horns are calculated to be plane within $1/16$ of a wavelength. Subsequent tests on the field patterns with both horns in place on the test section showed that 90 per cent of the field energy received by the detecting horn passed within a belt extending one wavelength beyond the geometrical aperture of the horns along the axis of the test section. Collimation in the E dimension was very good since very little signal could be detected outside of the test section in the E plane.

The second part of the problem was solved by confining the ionized gas flow in a rectangular, dielectric test section made of pyrex. The test section walls were reduced to effective half-wave plates by adding to the outer surfaces of the walls pieces of dielectric material tailored to make the combination of wall plus matching element reflectionless. Jahn⁽¹⁴⁾ has shown that reduction of the container walls to effective half-wave plates reduces the problem to the simple slab problem. The tailoring method used was to cut a series of rectangular slots across the face of the matching pieces in the direction perpendicular to the E vector (refer to Fig. 7). By a trial and error procedure the net reflection of the pyrex walls and matching pieces was reduced to about one per cent.

The two microwave circuits used in this experiment are shown in Fig. 8. The transmitted amplitude was measured by a

tunable crystal detector attached to the receiving horn. The reflected amplitude was measured during part of the experiments by a crystal detector on a directional coupler as shown. It was also measured using a matched magic tee in the balanced arm circuit also shown in Fig. 8.

Since this experiment was conducted primarily for low electron densities the reflected phase was not used. The transmitted phase was measured in a unique way that differed from the normal interferometer circuits. After the directional coupler circuit had been matched as closely as possible, a small mismatch was introduced at the transmission termination. A second disturbance was then added by the stub tuner preceding the first horn, of such a size and phase that it just canceled the other, making the ambient signal zero as seen by the reflection detector on the directional coupler. Subsequent introduction into the test section of a gas of electron density so low that no reflection occurs, produces a phase change in the small signal which returns through the gas from the far mismatch which is sufficient to unbalance the original null at the reflection detector. Thus, as the electron density increases, the response of the reflection detector is a series of periodic maxima and minima which are observable before the actual reflection from the gas becomes significant.

The electron densities for the occurrence of these maxima and minima are calculated in the following way. Consider the idealized circuit shown in Fig. 9 where r_1 is the reflection due to the stub tuner, r_2 is due to the reflection from the first air-glass-gas interface, r_3 is due to the reflection from the second ionized gas-glass-air interface,

and r_4 is the reflection due to the transmission termination. We can combine these elements by letting $R_1 = r_1 + r_2$ be everything not going through the gas, $R_2 = r_3 + r_4$ be everything going through the gas, and R be the net reflection seen by the detector. Initially R_1 and R_2 are equal in amplitude and phase so that R is zero. R_1 , R_2 , and R are related by the following relation:

$$R^2 = R_1^2 + R_2^2 - 2R_1R_2 \cos \Delta \phi \quad (33)$$

In general, continuing the assumption that significant $\Delta \phi$ occurs before R_1 changes,

$$R_2 = R_1 \exp(-2k_1 d) \approx R_1 T^2 \quad (34)$$

Thus,

$$R^2 = R_1^2 (1 + T^4 - 2T^2 \cos \Delta \phi) \quad (35)$$

To find the maxima and minima in $R^2(\Delta \phi)$, differentiate (35).

$$\frac{d(R/R_1)^2}{d(\Delta \phi)} = 2T^2 \frac{d(T^2)}{d(\Delta \phi)} - 2 \frac{d(T^2)}{d(\Delta \phi)} \cos \Delta \phi + 2T^2 \sin \Delta \phi = 0 \quad (36)$$

$$\begin{aligned} \text{or, } \sin \Delta \phi &= \frac{1}{T^2} \frac{d(T^2)}{d(\Delta \phi)} (\cos \Delta \phi - T^2) \\ &= \frac{d(\ln T^2)}{d(\Delta \phi)} (\cos \Delta \phi - T^2) \end{aligned} \quad (37)$$

Evaluating $d(\ln T^2) / d(\Delta \phi)$ from typical data we find a value of approximately -0.15 . Knowing the T^2 at which the maxima and minima occur we solve for $\Delta \phi$ to find the first few points:

$$\Delta \phi_{\text{max}} = 2.906, 9.240, \dots$$

$$\text{and } \Delta \phi_{\text{min}} = 6.193, 12.435, \dots$$

Now relate $\Delta\phi$ to the change in electron density in the following way:

$$\begin{aligned}\Delta\phi &= 2\pi \left(2d/\lambda_0 - 2d/\lambda \right) = 2d(k_0 - k_r) \\ &= 2dk_0(1 - K_r)\end{aligned}\quad (38)$$

Solving for K_r ,

$$K_r = 1 - (\Delta\phi/2)(\lambda_0/2d) \quad (39)$$

where $\lambda_0/2d = 1/8$ for our case. K_r is related to the electron density in the following way:

$$n = 7.146 \times 10^{12} (1 - K_r) \left[1 + (v_c/\omega)^2 \right]. \quad (40)$$

Thus, n is known as a function of $\Delta\phi$ and v_c/ω .

3. Interpretation of Experimental Data.

This experiment then consists of monitoring the reflection, transmission, and phase shifts of the microwave beam as functions of time after passage of the shock wave. A tracing of a typical oscilloscope record of the microwave response is shown in Fig. 10. The upper beam records T^2 , R^2 , and ten times R^2 using a type M Tektronix amplifier plug-in. A photocell was used to determine the arrival of the shock wave at the microwave horns and is usually recorded on the lower beam (not shown). The reflected signal first exhibits the small interference bumps described above as the electron density increases behind the shock wave before the reflected magnitude itself has become appreciable. It can be seen from the tracing that the reflected amplitude becomes significant only after T^2 has reached zero. Using Figures 3 and 4, v_c/ω can be estimated for the particular gas and Mach number range under study. The precise value of v_c/ω required is

determined by the following matching technique. Since ϕ_T is relatively insensitive to v_c/ω , a graph of n versus t (shown in Fig. 11) is begun with points calculated from the observed positions of the little maxima and minima in the early portion of the reflection trace using the estimated value of v_c/ω . The R^2 response is then reduced for a range of v_c/ω values near the estimated value and the resulting curves are added to the n versus t plot shown in Fig. 11. It can be seen that the curves emerge from a common value of n at the lowest detectable R^2 . Finally, the T^2 response is also reduced for these same values of v_c/ω and then the T^2 curve is selected which best overlaps the ϕ_T bump points for low n and extrapolates through the corresponding R^2 curve for the higher n . This curve fitting is found to be quite unambiguous. If a different value of v_c/ω is chosen, the T^2 curves would deviate noticeably from the end points and slopes established by the ϕ_T and R^2 curves for the same value of v_c/ω . The value of v_c/ω chosen was found to be almost constant for data taken with the same gas at a constant initial pressure even though the temperature range was quite broad. This composite curve is then the uncorrected n versus t variation for a given test run. The next step is to correct the measured quantities to account for experimental departures from the plane wave- plane slab idealizations.

The first correction involves the crystal diodes used to measure the microwave energy. Ideally, the crystal detectors are square law, but in practice the detectors respond only approximately to the square of the local field amplitude and must be calibrated in place at the signal level, carrier frequency, and response frequency typical of the actual data. This calibration was accomplished by

using a precision attenuator in the microwave circuit (shown in Fig. 8) and results in the typical curve shown in Fig. 12 for the transmission crystal. A similar curve results for the reflection crystal. The data points shown are for several calibrations taken at periodic intervals of time over a period of three years. Essentially the crystal response characteristics remained constant within a few per cent under the operating conditions of this experiment. This is not always true so that one must be extremely cautious in applying crystal detector corrections.

Next consider the corrections for the deviations of the probing field from a plane wave. The main complication introduced by a curved wave front is its vulnerability to refraction resulting in a reduction of the transmitted signal. The first refraction effect arises from the distortion of the radiation patterns of the two horns by the introduction of a gas of lower index of refraction into the test section. Lacking any permanent media of refractive index lower than one with which to calibrate the probe against this effect, theoretical calculations of near field horn patterns⁽²⁰⁾, which indicate that the field intensities on the horn axis in this region scale as the product of wavelength and axial distance from the horn mouth, were used to estimate the refraction losses. A series of calibrations were then made in which the received signals were obtained as a function of horn separation. From this and the relations between λ and T^2 given in the slab calculations, the refraction losses were calculated. Fig. 13 shows the resulting plot of change in power received by the receiving horn as a function of distance between the two horns. The actual field pattern intensity oscillated quite rapidly with slight

changes in separation distance when the horns were separated by a distance less than approximately four wave lengths. The mean curve of this intensity envelope was used to correct the transmission characteristics. The correction involved varied from zero at $T^2 = 0$ and 1.0 to about five per cent of the total transmission at an intermediate value, small enough to justify the somewhat cavalier treatment of it in this situation. For less favorable geometries, or less well collimated horn fields, more detailed calibration against this effect could be required. Referencing the change in decibels to $d = 5$ cm, the correction was applied as follows. Knowing the relationship between λ and electron density n (or between k and n , Eqn. (23)), for a given electron density in the test section the spacing between the horns, x , can be determined and the change in decibels calculated, where,

$$\Delta DB = (DB)_x - (DB)_{d=5 \text{ cm}} \quad (41)$$

Then using the relation between ΔDB and T^2 ,

$$\Delta DB = 10 \log (T/T_0)^2 \quad (42)$$

the correction to the transmission curves is then,

$$\Delta = 1 - (T/T_0)^2 \quad (43)$$

By applying the crystal correction and the horn separation correction to the T^2 and R^2 curves plotted in Figures 3 and 4, the curves for T^2 and R^2 become as shown in Figures 14 and 15 where S_T/S_{T_0} and $S_R/S_{R_{\text{total}}}$ are now the voltage ratios that are obtained from the oscilloscope records as a function of time.

Next, one must consider the deviations of the ionization profiles from a plane slab. The sensitivity of the probe to departures

from the assumed plane slab ionization profile, particularly ionization gradients in the direction of propagation, is clearly a crucial point. The obvious concern is that the gas dynamic boundary layers and/or the electrical boundary effects will replace the assumed discrete interfaces by smooth transition zones of sufficient depth to cause first order deviations from the plane slab solutions. Albini and Jahn⁽²¹⁾ have studied this problem in detail and found that the solutions for slabs bounded by transition zones in excess of about $0.2 \lambda_0$ differ significantly from those bounded by sharp interfaces. If the gas sample is more than a few wavelengths thick in the direction of propagation, R^2 is affected more than T^2 , since the latter responds mainly to the integrated path properties while the former responds mainly to the first surface. As this surface becomes more diffuse, R^2 decreases and T^2 increases. Specifically, for the dimensions and parameters given above, R^2 would be about twenty per cent lower and T^2 about five per cent higher in their mid-ranges if transition zones of $0.25 \lambda_0$ replaced the sharp interfaces.

Clearly then, the dependence of the measurables on the character of the boundary regions can lead to mis-interpretation of the free stream electron density and collision frequency. Unfortunately, the estimation of the boundary layer thicknesses are seldom straightforward and calculation of their detailed profiles is usually impossible. The gas dynamic boundary layer profile is pertinent only if local ionization equilibrium prevails through it. The electron density profile due to ambipolar diffusion to the test section wall is more appropriate but more difficult to evaluate because of uncertain atomic cross-sections in the regions of temperature gradient and unknown electrical boundary

conditions at the wall surface. In this experiment, boundary layer⁽²²⁾ and ambipolar diffusion⁽²³⁾ calculations were used to determine the upper limits for boundary layer thicknesses large enough to alter the R^2 and ϕ_T significantly. For a laminar boundary layer and a shock speed of 2×10^5 cm/sec, at 250 μ sec after passage of the shock front, the boundary layer thickness is calculated to be approximately 0.25 cm which is clearly lower than the critical limit of $0.25 \lambda_0$. For even the weakest shocks, the laminar boundary layer thicknesses were calculated to be below about $0.2 \lambda_0$ in all cases for times less than about 200 μ sec. By restricting ourselves to laboratory times less than about 200 μ sec in all cases and below 100 μ sec in most cases, the effect of these boundary layers can usually be neglected in the study of initial ionization rates. The manifestation of this boundary layer effect would be a drooping of the n versus t curves deduced from the measurables R^2 and ϕ_T below the composite curve in Fig. 11 for long times in the flow behind the shock when the boundary layer thicknesses have become large. Such behavior is indeed seen in isolated instances, but never enough to justify alteration of the composite curve.

Since a gradient in electron density also exists in the axial direction behind the shock wave, the microwave beam could be refracted in the axial direction causing the measured T^2 to be reduced. Considering an idealized two dimensional picture, the radius of curvature R is related to the index of refraction in the usual way:

$$1/R = (1/\mu) dp/dx \quad (44)$$

where the index of refraction is defined as

$$\mu = c/v_p = ck_T/\omega = k_T/k_0 \quad (45)$$

The real part of the propagation exponent was defined previously in terms of ω_p/ω and v_c/ω ,

$$K_r = k_r/k_0 = [1 - (\omega_p/\omega)^2]^{1/2} + O(v_c/\omega) \quad (46)$$

where the plasma frequency is related to the square root of the electron density:

$$\omega_p = 5.64 \times 10^4 (n)^{1/2} \quad (47)$$

Then,

$$d\mu/dx \approx 7 \times 10^{-14} dn/dx \quad (48)$$

Consider an extreme case where $n(x)$ goes linearly from 0 to $3 \times 10^{12} \text{ cm}^{-3}$ across the geometrical aperture (which would be the case approached in the neighborhood of shock Mach number 10 which is not reached in this experiment). This would then give,

$$d\mu/dx \approx 0.1 \text{ cm}^{-1}$$

Then,

$$R = \mu / (d\mu/dx) \lesssim (d\mu/dx)^{-1} = 10 \text{ cm} \quad (49)$$

The deflection of the center of the beam at the far side of the test section would then be approximately 2.5 cm which is equivalent to approximately one horn aperture at this extreme case. This deflection of the microwave beam would ^{cause} the measured T^2 to be smaller than it should be and as a result, the T^2 curve would deviate slightly below the composite curve. In a few shots into krypton where the Mach number was extremely high, above Mach number ten, this slight drooping of T^2 below the composite curve was observed. This data was not considered in any of the calculations and does not appear in any of the presented results and is mentioned only to show that this effect does become extremely important at very high electron density gradients.

Having now considered the influence of the deviations from the ideal microwave probe on the electron density distribution, the non-ideal conditions existing in the shock tube which might influence the experimental results must be discussed. The electron density distribution as a function of time, obtained from the microwave records on the oscilloscope record, must be corrected to account for the fact that the shock wave is decelerating as it travels down the tube.

V. SHOCK ATTENUATION

The electrons that are measured by the microwave probe began life a considerable distance up the tube from the test section. Since the heated gas is hotter behind the shock wave up the tube from the test section, the resulting electron densities are higher than if the gas had been heated at the test section. Since it is desirable to reference the measured electron densities to the test section conditions, the temperature history behind the shock wave must be determined.

By measuring the shock wave arrival times at several positions along the tube, the shock attenuation can be determined and consequently the electron density correction. The shock wave arrival time at a given position along the tube was determined from the rise in amplitude of film gauge records. On some of the runs, two crystal counters were used to give additional data and to check

the data obtained from the oscilloscope records. This film gauge method is thought to be adequate for Mach numbers below about 8.5. Above this Mach number the film gauge trace goes negative before going positive. The positive amplitude is due to the rise in temperature behind the shock while the negative dip at high Mach numbers may be due to precursor electrons since the characteristics of the negative dip correspond to oscilloscope traces taken by A. J. Kelly⁽²⁴⁾ in observing precursors by means of a gauge on the side wall of the shock tube. The negative dip of the film gauge record was present even in the absence of a driving current so that the effect is an electromagnetic one and is not entirely due to a shorting of the gauge. Above Mach number 8.5, the value of the shock attenuation was determined by using the points where the film gauge traces went positive. Attenuations using this technique agreed quite well with expected values from comparable shock tubes at the same conditions and with extrapolated data from the runs below Mach number 8.5. From this information the electron density correction can be determined and applied to the measured $n(t)$ curves. The temperature history correction to the electron density was carried out in the following manner. Assume as a first approximation that the simple shock tube theory applies with the conventional x, t diagram as shown in Fig. 16. Also assume that a small volume of gas, passed over at the position x_1 by a shock wave of Mach number M_1 , remains at the temperature T_1 as it flows by the test section. Since the time difference $t'_1 - t_0$ is the time measured in the laboratory and $T_0 = T_0(M_0)$ is the calculated temperature at

the test section, let the temperature T_1 be expressed in terms of these known quantities. All temperatures are in region 2 behind the shock wave. Expanding T_1 in terms of the test section conditions,

$$\begin{aligned} T_1 (M_1 [x_1(t_1^*)]) &= T \{ M_0 + (dM/dx)(x_1 - x_0) \} \\ &= T \{ M_0 [1 + (1/M_0)(dM/dx)(x_1 - x_0)] \} \end{aligned} \quad (50)$$

where the brackets denote that the temperature behind the shock wave is evaluated at the shock Mach number given in the brackets.

Let $A = (1/M_0)(dM/dx)$ be the shock attenuation per meter and rewrite in terms of the laboratory time behind the shock, $t_1^* - t_0$. From Fig. 16,

$$\begin{aligned} x_1 - x_0 &= V_s (t_0 - t_1^*) \\ &= V_s [(t_1^* - t_1) - (t_1^* - t_0)] \end{aligned} \quad (51)$$

$$\text{and, } x_1 - x_0 = V_2 (t_1^* - t_1) \quad (52)$$

Eliminating $(t_1^* - t_1)$ between the two expressions,

$$x_1 - x_0 = \frac{V_s}{V_s/V_2 - 1} (t_1^* - t_0) \quad (53)$$

From shock relations,

$$V_2 = V_s - u_2 = V_s \left(1 - \frac{\rho_1}{\rho_2} \right) \quad (54)$$

so that,

$$\frac{V_s}{V_2} - 1 = \frac{1}{\rho_2/\rho_1 - 1} \quad (55)$$

But,

$$\frac{\rho_2}{\rho_1} = \frac{(\gamma + 1) M^2}{(\gamma - 1) M^2 + 2} = \frac{4 M^2}{M^2 + 3} \quad \text{for } \gamma = 5/3$$

Thus, we arrive at the desired result,

$$T_1 = T \left\{ M_0 \left[1 + AV_s \frac{3M_0^2 - 3}{M_0^2 + 3} (t_1' - t_0) \right] \right\}. \quad (56)$$

Assuming a bi-atomic process as the dominant process, the rate of ionization is given by,

$$\dot{n} = C T^\xi \exp(-E_a/kT) \quad (57)$$

where C is a constant dependent on the number of particles per cubic centimeter and the molecular weight and ξ is the temperature exponent which is $3/2$ for the choice of cross-section used in this paper.

Particles passed over at position x_1 by the shock wave are assumed to remain at temperature T_1 , so that when they pass the test section at time t_1' the ionization level is

$$n_1(t_1') = \int_{t_1}^{t_1'} \dot{n}_1 dt = C T_1^\xi e^{-E_a/kT_1} (t_1' - t_1). \quad (58)$$

Had the shock wave remained at uniform strength corresponding to its value at the test section, ionization would have been lower, namely,

$$\bar{n}_1(t_1') = A T_0^\xi (t_1' - t_1) \exp(-E_a/kT_0) \quad (59)$$

so that,

$$\frac{\bar{n}_1}{n_1} = \frac{T_0^\xi}{T_1^\xi} \exp\left[\left(\frac{E_a}{k} \right) \left[\frac{1}{T_1} - \frac{1}{T_0} \right] \right]. \quad (59)$$

Since the exponential term is dominant and $(T_0/T_1)^\xi \approx 1$ for the temperature range in this experiment, the ratio of the temperatures was neglected for purposes of this correction.

The procedure used for the attenuation was then to measure the shock velocity, calculate T_0 and T_1 (Δt_{lab}^*) using the measured shock attenuation factor A and then correct $n_1(t_1^*)$, which is the measured electron density, to the true electron density growth $\bar{n}_1(t_1^*)$. The procedure outlined above and used in this experiment was able to determine shock arrival times within one microsecond which gave an error in the calculated temperature T of approximately 50°K . This uncertainty in temperature corresponds to a maximum error of less than 15 per cent in the electron density correction.

Besides the uncertainty in the calculated temperature at the test section, there is also the uncertainty in determining the attenuation factor that appears in the correction. An error in determining this within a factor of two for a given data point could introduce a maximum error of approximately five per cent in the electron density correction. Thus the total electron density error could be about twenty per cent under the worst possible conditions. However, since most of the plots used in the interpretation of the data involve $\log_e n$ the points would be shifted at most 0.22 units on the curve shown in Fig. 19.

The uncertainty in temperature history would account for some of the scatter in the data and may account for the weak pressure dependence which will be discussed later. For most of the experimental points the uncertainty is not as large as the numbers quoted above and certainly not large enough to cause significant changes in the final experimental results.

VI. RESULTS

1. Argon

The electron density growth, $n(t)$, as a function of time after passage of the shock wave is linear from the origin (as shown in Fig. 17) where the origin is defined as the earliest measurable time. The fact that the curves are linear supports the assumption that the atom-atom collisional phase is the relevant process for the temperature range and time scales considered in this experiment. Since it will be shown later that the two step atom-atom collisional process is the relevant one, we can attach some significance to the fact that the curves are linear from the origin. This means that the initial induction period for the build-up of the steady-state A^* population is shorter than the earliest measurable time of this experiment. The earliest measurable time is equal to the time that the shock wave requires to pass from one edge of the microwave horn radiation pattern to the other edge. Typically, this passage time is of the order of one microsecond, so that the induction period must be less than one microsecond.

Absolute rates of ionization are very slow. It takes approximately 100 μ sec to reach the electron-atom collisional phase (point where the atom-atom ionization rate equals the electron-atom ionization rate) at 9000°K in argon as shown in Fig. 18. For 8000°K , it takes approximately 450 μ sec to reach the electron-atom phase. For 6500°K , the time required would be about 88 millisecc. Since the testing time available in the shock

tube are generally shorter than the required times to reach the electron-atom phase for test gas temperatures below about 8000°K, the observed $n(t)$ curves are linear throughout the testing period. Absolute rates of ionization varied from approximately 1.5×10^{13} to $7.5 \times 10^{16} \text{ cm}^{-3} \text{ sec}^{-1}$ over the range of temperatures between 5500°K and 9600°K.

Fig. 19 shows a plot of $\ln h$ as a function of $1/kT$ for the initial test pressure of 5 mm Hg in argon. Using Eqn. (12), the activation energy, E_a , was calculated at a value of $kT = 2/3 \text{ ev}$ and found to be $11.9 \pm 0.5 \text{ ev}$. Well within the experimental error, this value coincides with the first excited electronic state value of 11.55 ev⁽²⁵⁾ rather than the first ionization potential of 15.75 ev. This is strong evidence for the two step atom-atom collisional process being the dominant process for the temperature range considered.

The pressure sensitivity of the ionization reaction is so mild in comparison with the exponential temperature dependence (Eqn. 11) that the pressure dependence tends to be obscured by the random fluctuations introduced in the data by slight variations in impurity level and by uncertainties in the thermal history, i. e., attenuation of the shock wave. Fig. 20 shows the pressure dependence for argon obtained for the very purest experiments. Within an admittedly broad uncertainty, the electron density growth, h , is proportional to the pressure squared.

The results quoted above were derived from the purest ambient gases obtainable to date with the pumping and flow system

described previously. Earlier data, taken with lower purity gas, differs from this in the absolute values of the ionization rates and in the apparent activation energy extracted from the semi-log plots in amounts depending on the specific purity level. As shown in Fig. 21 for the case of argon, as the impurity decreased from about 100 parts per million to ten parts per million, the absolute level of the ionization rate decreased while the activation energy remained essentially constant at a value of 6.3 ev, which is significantly below the first excited state in argon. It was not until the impurity level was reduced to 0.1 to 5 parts per million that the activation energy and the levels of ionization quoted above were obtained.

During the course of the experiments, the flow system underwent several modifications when preliminary data gave results depending on the specific impurity levels. The three flow systems that evolved are compared in the following table for argon at pressures of 3, 5, 10, and 13 mm Hg. The purity levels listed are based on perfect mixing of the impurity leaking into the research grade gas stream. The values listed for flow system III indicate that the impurities of the test gas will be due primarily to the impurity level of the research-grade gas. Flow system III was used for the majority of the experiments so that the results obtained are for gases of purities of one part in 10^7 . Increasing the flow rate by about a factor of three completely changed the experimental results, as can be seen by comparing Fig. 19 and Fig. 21. In order to insure that impurities were no longer significantly affecting the results, the flow rate was further increased by a factor of five. As can be seen from Fig. 19, flow systems II and III gave essentially

the same results for an initial pressure of 5 mm Hg.

FLOW SYSTEM COMPARISON TABLE

Flow System	$P_1 = 3$ mm Hg		$P_1 = 5$ mm Hg		$P_1 = 10$ mm Hg		$P_1 = 10^3$ mm Hg	
	F	I	F	I	F	I	F	I
I	1.8	7.0	2.87	4-7	---	----	10.1	1.2
II	---	----	6.9	2.5-3.0	---	----	26.6	0.7
III	26.9	0.5-1.0	35.2	0.2-1.0	95.4	0.1-0.2	----	---

$(F) \times 10^{15}$ = Flow Rate in particles/cc/sec

$(I) \times 10^{-6}$ = Impurity Level

Using the experimentally determined values of E_a , Eqn. (9) and Eqn. (11) were used to calculate the previously defined cross-sections Q_0 and C . The results of these calculations are shown in Fig. 22 and Fig. 23. The significant thing to notice is that both Q_0 and C decrease very rapidly with temperature, suggesting that a more exact cross-section should be chosen in Eqn. (7). Furthermore, the dependence with temperature appears to be exponential. An exponential form of the cross section was assumed and fitted to the experimental data. However, due to the fact that $kT \ll E_a$, there are very few atoms with relative energies greater than E_a . As a result, the tail-off of the cross-sections with energy cannot be obtained accurately enough from the experimental data to establish the parameters of the exponential cross-section. Also since the exponential temperature factor dominates the rate equations, the accurate determination of the magnitudes Q_0 and C again may be obscured by the random fluctuations of the data as was the case for the pressure dependence.

The cross-section Q_0 and the cross-section determined from the parameter C are defined with respect to the threshold energy and as a consequence include only colliding particles with relative energies greater than threshold. The definition of cross-section that may be more familiar involves all of the particles, even the ones with energies less than threshold, and is related to the rate of ionization in the following way:

$$\dot{n} = N^2 \bar{v} Q \quad (61)$$

where Q is now the "total" cross-section and $\bar{v} = (3kT/M)^{1/2}$ is the thermal velocity of the atoms. Using this equation to calculate Q from the experimentally determined rates of ionization, we arrive at the results shown in Fig. 24. The cross-section, Q , varies from approximately 10^{-27} cm^2 at $T = 5700^\circ\text{K}$ to $7 \times 10^{-25} \text{ cm}^2$ at 9600°K . Empirically, for the lower temperature data, Q appears to have an exponential temperature dependence given by

$$Q \approx 2 \times 10^{-21} e^{-7.2/kT} \text{ cm}^2 \quad (62)$$

It is of interest to note that the cross-section Q for argon is less than the cross-sections for krypton and xenon as one would intuitively expect, but that the cross-section parameters Q_0 and C for argon are greater than those for krypton and xenon.

2. Krypton.

The $n(t)$ curves for krypton are linear from the origin, as shown in Fig. 25, again supporting the assumption that the atom-atom process is dominant. The rates of ionization for krypton are also relatively slow, but are faster than the rates in argon. For a gas

temperature of 9000°K , the electron-atom phase is reached in approximately $60\mu\text{sec}$, while for 8000°K , the time required is $200\mu\text{sec}$. The available testing time in krypton is significantly longer than for argon, allowing lower temperature experiments to reach the electron-atom phase. Absolute rates of ionization varied from approximately 0.05 to $3.5 \times 10^{16} \text{ cm}^{-3} \text{ sec}^{-1}$ over the range of temperatures considered.

Fig. 26 shows a plot of $\ln i$ as a function of temperature for the initial pressure of 5 mm Hg. Using Eqn. (12), the activation energy was calculated for $kT = 2/3 \text{ ev}$ and was found to be $10.4 \pm 0.5 \text{ ev}$ which coincides with the first excitation potential value of 9.92 ev rather than the first ionization potential value of 13.99 ev . As in the case of argon, this indicates a preference for the two-step process rather than the one step process.

Again, as shown by the data in Fig. 27, within experimental error, a pressure dependence of P^2 is obtained. The solid curves indicate a theoretical spacing of P^2 from the 5 mm Hg.

Gas purity also plays an important role in the case of initial rates of ionization in krypton. Mass spectrographically analyzed krypton was used in the experiments. Impurity levels of the gas were of the order of one part in 10^7 . Several tests were made to determine the rates of ionization for no flow at initial pressures of 10 and 17 mm Hg. The results are presented in Fig. 28. The rate of ionization was increased almost by a factor of four while the activation energy remained constant. Thus some unknown impurity increased the rate of ionization for the no flow condition over the flow conditions. The rate controlling mechanism, the excitation of the krypton atoms, remained the same.

Quite by accident, a controlled impurity experiment was conducted during the 5 mm Hg series of tests. Tests using a borrowed cylinder of research grade krypton yielded a much higher rate of ionization than tests using other cylinders. Upon analysis, the cylinder was found to contain 1.59 per cent benzene. Results of this series of tests are presented in Fig. 29. The rate of ionization was increased by a factor of almost 70 by the addition of the benzene, while the activation energy remained essentially the same as in the purest cases.

Figures 30 and 31 show the magnitudes of the cross-section parameters obtained from Equations (9) and (11) for Q_0 and C . Again as in the case for argon, Q_0 and C decrease very rapidly with temperature. Q_0 varied from 0.8 to $3.3 \times 10^{-19} \text{ cm}^2$ and C varied from 0.9 to $4.0 \times 10^{-19} \text{ cm}^2/\text{ev}$. As for the argon case, C and Q_0 appear to depend exponentially on the temperature. The cross-section for all particles, Q , defined by Eqn. (61) is found to vary from $7 \times 10^{-27} \text{ cm}^2$ at 6000°K to $2.5 \times 10^{-25} \text{ cm}^2$ at 8000°K . As shown in Fig. 24, Q appears to have an exponential temperature dependence given approximately by

$$Q \approx 1.2 \times 10^{-20} e^{-7.4/kT} \text{ cm}^2 .$$

3. Xenon.

As shown in Fig. 32, the initial electron density curves are linear in time from the origin indicating that the initial ionization is again due to atom-atom collisions in the gas. At the highest temperature levels of this experiment, the electron-atom phase was reached very rapidly and the rate of ionization observed is

probably due to a combination of the excitation-ionization process and the electron-atom process. The electron densities plotted here are only the part due to the atom-atom phase where the $n(t)$ values are taken from the mean curve for 5 mm Hg in Fig. 33.

The rates of ionization in xenon are considerably faster than those in argon or krypton. Absolute rates of ionization in xenon varied from about 0.1 to $10 \times 10^{16} \text{ cm}^{-3} \text{ sec}^{-1}$ for the temperature range considered. Ionization rates were obtained only for the case of the best flow system and for the highest purities using Linde mass-spectrometer analyzed xenon.

Fig. 33 shows a plot of $\ln \dot{n}$ as a function of temperature for the initial pressure of 5 mm Hg. Using Eqn. (12) the activation energy E_a for xenon at $kT = 0.57 \text{ ev}$ was found to be approximately $8.6 \pm 0.6 \text{ ev}$ which again coincides with the first excited electronic state value in xenon of 8.32 ev rather than the first ionization potential value of 12.13 ev. This value strongly supports the choice of the two step atom-atom collisional mechanism given in Eqn. (2) rather than the one step mechanism given in Eqn. (1).

The pressure dependence in xenon may or may not be P^2 . The data is insufficient to determine the pressure dependence. On the basis of the few points that are shown in Fig. 34, within experimental error, there is nothing that suggests a dependence other than P^2 .

Figures 35 and 36 show the variation of the magnitude of the cross-section parameters Q_0 and C obtained from Equations (9) and (11) respectively. Again it is seen that Q_0 and C vary significantly with temperature. Q_0 ranges from $0.7 \times 10^{-20} \text{ cm}^2$ at $T = 8800^\circ \text{K}$ to $1.8 \times 10^{-20} \text{ cm}^2$ at 6000°K , while C varies from $2.3 \times 10^{-20} \text{ cm}^2/\text{ev}$ at

$T = 8800^{\circ}\text{K}$ to $6.5 \times 10^{-20} \text{ cm}^2/\text{ev}$ at 6000°K . The lines in Figures 35 and 36 indicate that the variation of Ω_0 and C are almost exponential with temperature.

The cross-section Ω defined by Eqn. (61) was found experimentally to vary from $5 \times 10^{-27} \text{ cm}^2$ at 5500°K to $3 \times 10^{-24} \text{ cm}^2$ at 8800°K as shown in Fig. 24. In a very approximate manner, Ω is found to have an exponential temperature dependence given by

$$\Omega \approx 5 \times 10^{-20} e^{-7.6/kT} \text{ cm}^2$$

The cross-section for all particles, Ω , is thus very small for this range of temperatures and re-emphasizes the fact that the rates of ionization for the three noble gases, argon, krypton, and xenon are extremely small.

VII. CONCLUSIONS

For temperatures of 5500°K to 9600°K behind shock waves in argon, krypton, and xenon, the initial ionization is found to result from a two-step collisional process which involves the first excited electronic state. The choice of this process is supported by the following experimentally determined facts:

1. The initial electron density growth with time behind the shock wave is linear from the origin.
2. The slope of the Arrhenius plot $\ln \dot{n}$ versus temperature yields an activation energy that is near the first excited state potential for each gas.
3. The rate of ionization \dot{n} is proportional,

within experimental limitations, to P^2 or N^2 as predicted by theoretical considerations.

Purity of the test gas was found to strongly influence the absolute initial rates of ionization of the three gases and to strongly affect the activation energies, particularly in the case of argon.

Shock attenuation was found to be an extremely important parameter in determining the correct electron density growth with time. Very small uncertainties in the temperature history of the shock-heated particles causes large uncertainties in the absolute electron density measurements.

REFERENCES

1. Ramsauer, C., Annalen der Physik, (1921), Vol. 64, pp. 513-540, (1921) Vol. 66, pp. 546-558, (1923) Vol. 72, pp. 345-352.
2. Townsend, J. S., and Bailey, V. A., Phil. Mag. (1922) Vol. 43, pp. 593-600.
3. Brode, R. B., Phys. Rev. (1925) Vol. 25, pp. 636-644.
4. Ramsauer, C. and Kollath, R., Annalen der Physik (1929) Vol. 3, pp. 536-564.
5. Normand, C. E., Phys. Rev. (1930) Vol. 35, pp. 1217-1225.
6. Massey, H. S. W. and Burhop, E. H. S., Electronic and Ionic Impact Phenomena, Oxford (1952).
7. Petschek, H. and Byron, S., Annals of Physics (1957) Vol. 1, pp. 270-315.
8. Weymann, H. D., University of Maryland Institute for Fluid Dynamics and Applied Mathematics TN BN-144 (1958).
9. Sturtevant, B., Physics of Fluids (1961) Vol. 4, pp. 1064-1073.
10. Chapmann, S. and Cowling, T. G., The Mathematical Theory of Non-Uniform Gases, The University Press, Cambridge, (1952).
11. Von Engle, A., Ionized Gases, The Clarendon Press, Oxford, (1955).
12. The author is indebted to Mr. A. L. Ayers of ALCOA for his personal interest in the preparation of this unusual extrusion.
13. Professor D. Morelli and his students designed and implemented the mechanical details of the tube and its suspension.
14. Jahn, R. G., Guggenheim Jet Propulsion Center, California Institute of Technology, TN - 2 (1960).
15. Jahn, R. G., Physics of Fluids, (1962) Vol. 5, pp. 678-686.
16. Schultz, D. L., Colston Papers, Butterworths Scientific Publications, London (1958), Vol. XI.
17. Kivel, B., Avco-Everett Research Note 129 (1959).

18. We are indebted to the Western Data Processing Center at UCLA.
19. Borgnis, F. E., and Papas, C. H., in Handbuck der Physik edited by S. Flugge, Springer Verlag, Berlin (1958), Vol. XVI.
20. Harris, F. G., Rome Air Development Center TN - 58-252 (1958).
21. Albini, F. A., and Jahn, R. G., J. Appl. Phys., (1961), Vol. 32, pp. 75-82.
22. Mirels, H., NACA TN 3401 (1955), NACA TN 3278 (1956), NACA TN 3712 (1956).
23. Brown, S. C., Basic Data of Plasma Physics, Wiley, New York, (1959).
24. Kelly, A. J., California Institute of Technology, Unpublished Communication, (1962).
25. Cook, G. A., (Editor), Argon, Helium, and The Rare Gases, Interscience, New York, (1961).

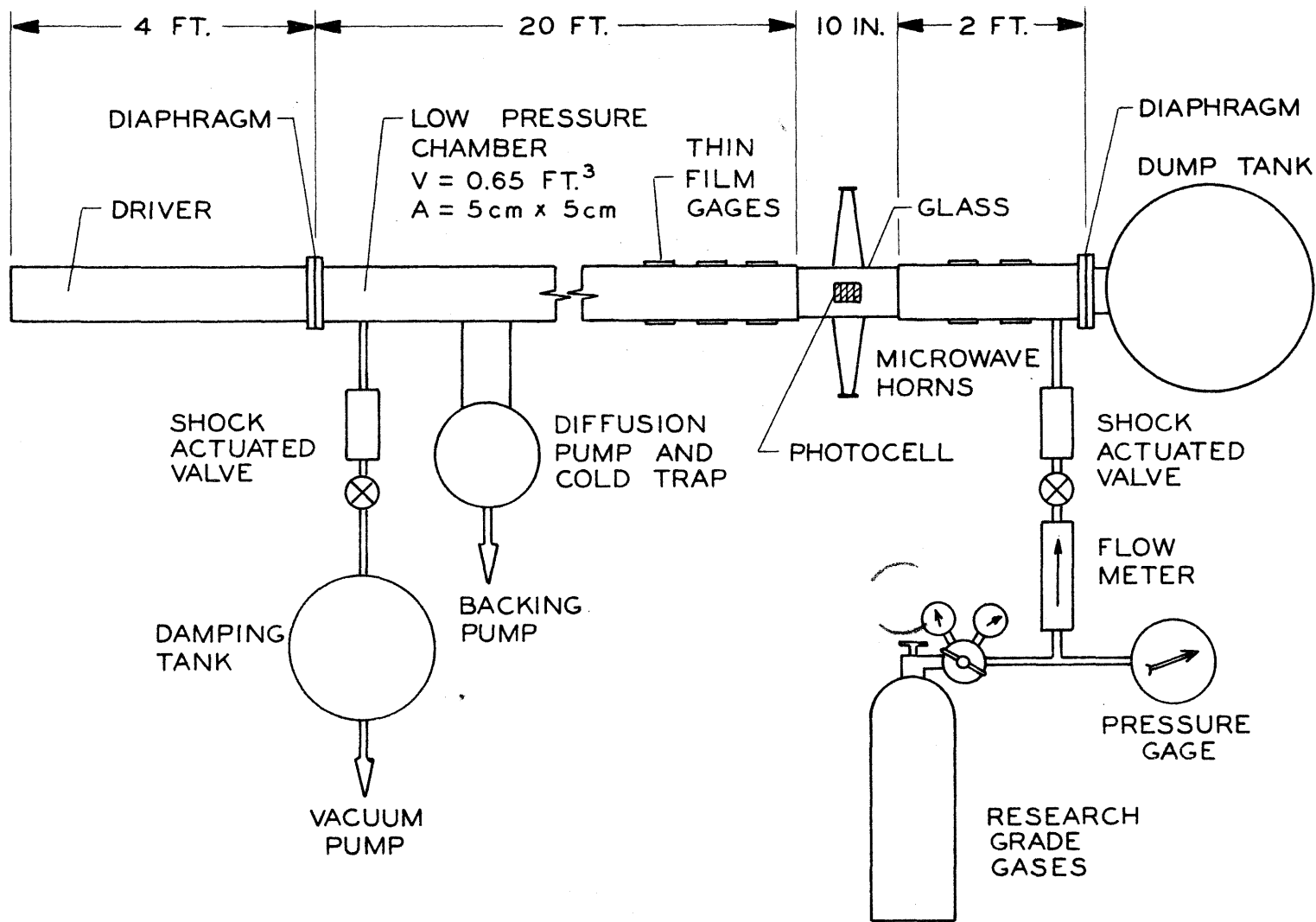


FIGURE 1 SCHEMATIC OF SHOCK TUBE AND FLOW SYSTEM

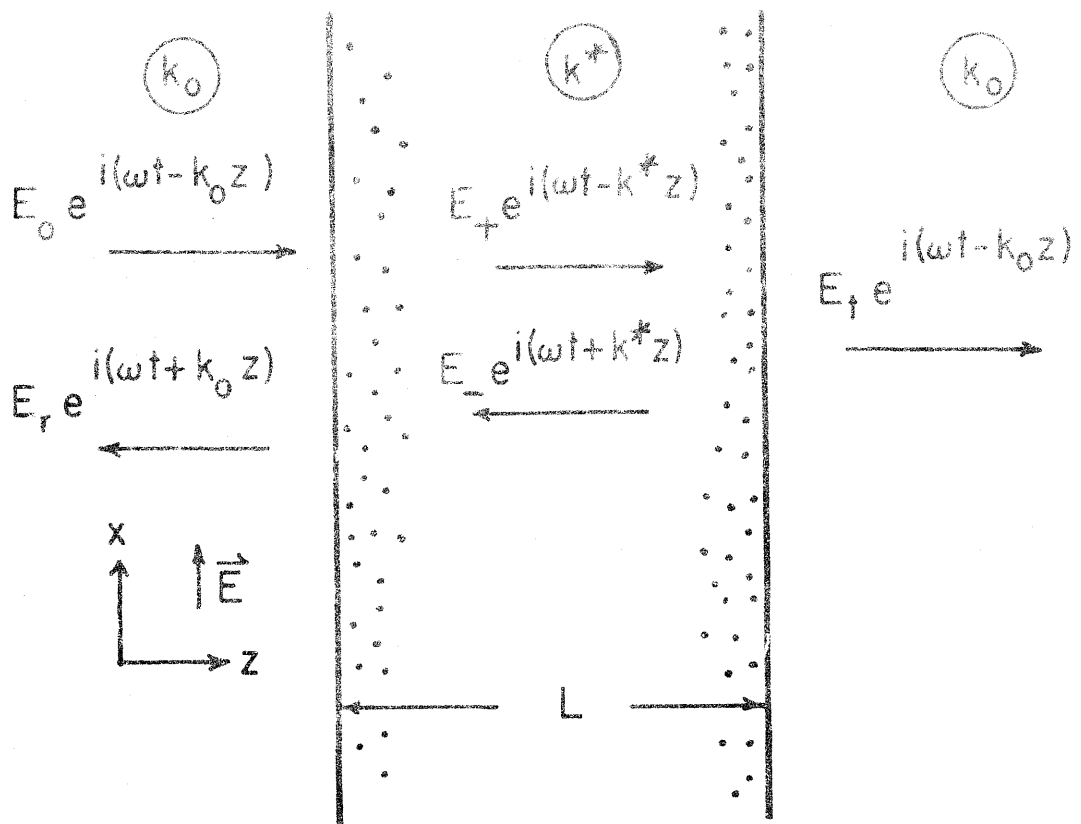


Fig. 2 Plane Wave - Plane Slab Interaction Geometry

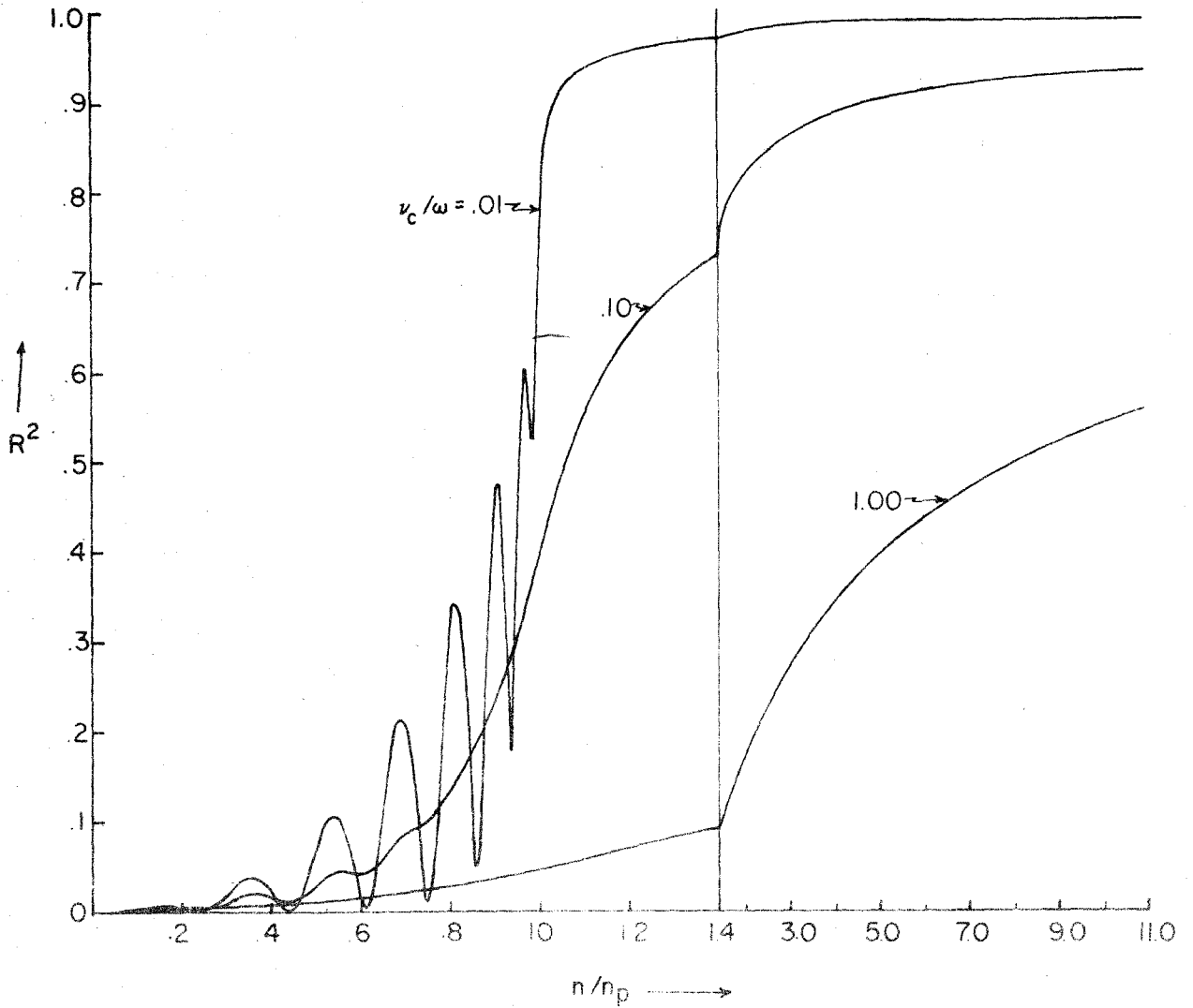


Fig. 3 Reflection from a Plane Slab of Ionized Gas, $L = 4 \lambda_0$

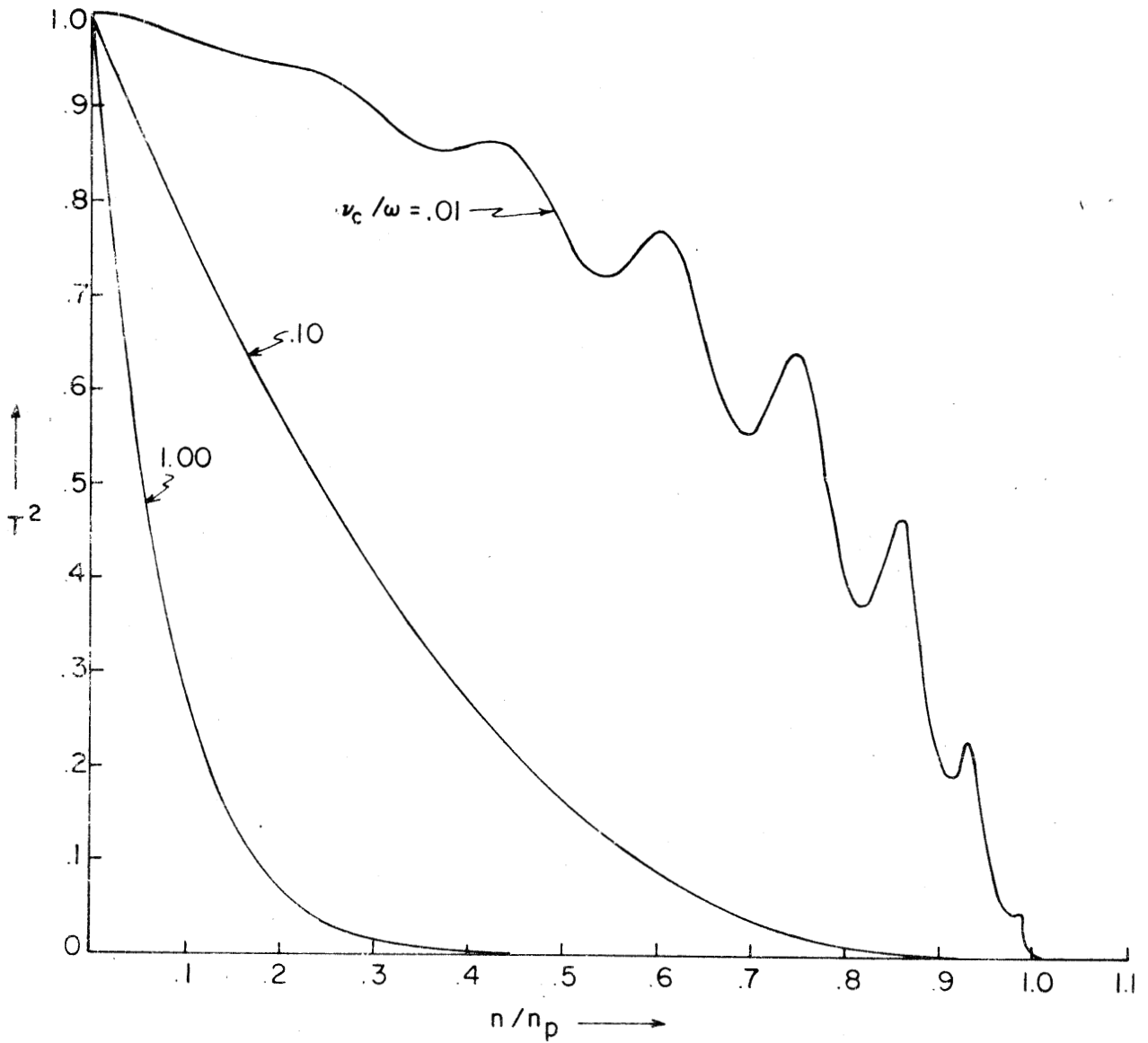


Fig. 4 Transmission through a Plane Slab of Ionized Gas, $L = 4 \lambda_0$

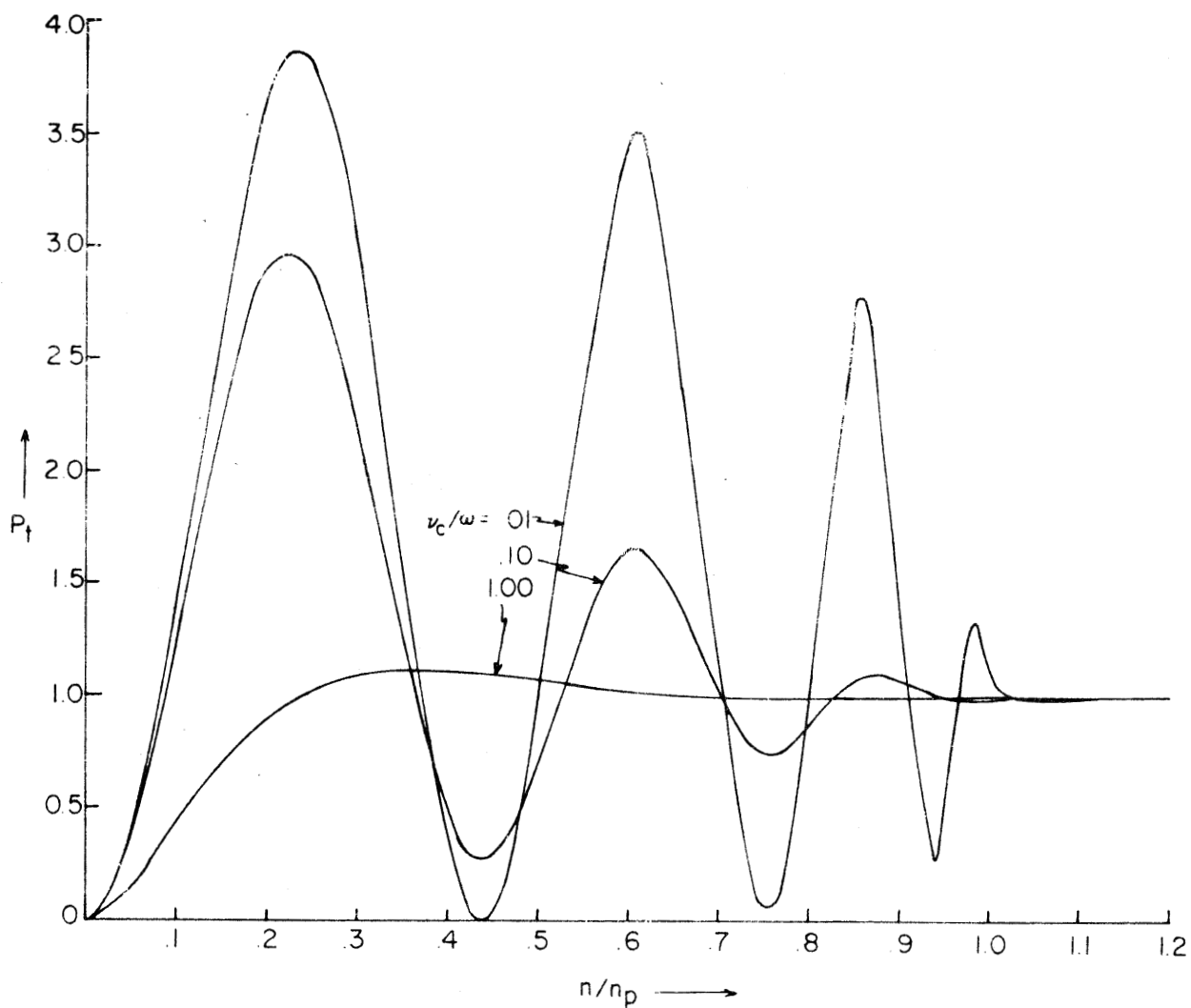


Fig. 5 Transmitted Phase Measurable, $P_t = 1 + T^2 - 2T \cos \phi_t$, for a Plane Slab of Ionized Gas, $L = 4 \lambda_0$

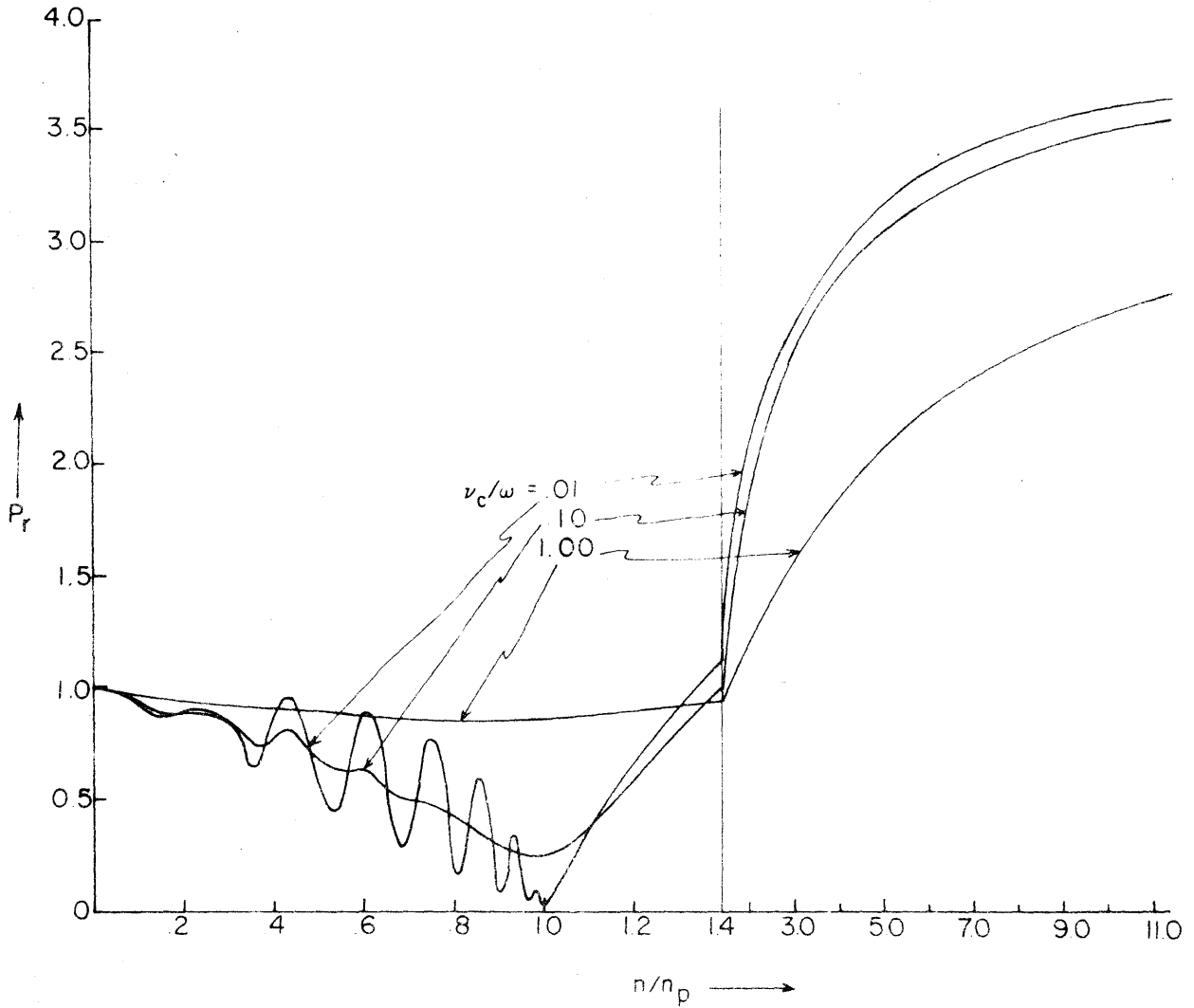


Fig. 6 Reflected Phase Measurable, $P_r = 1 + R^2 - 2R \cos \phi_r$, for a Plane Slab of Ionized Gas, $L = 4 \lambda_0$

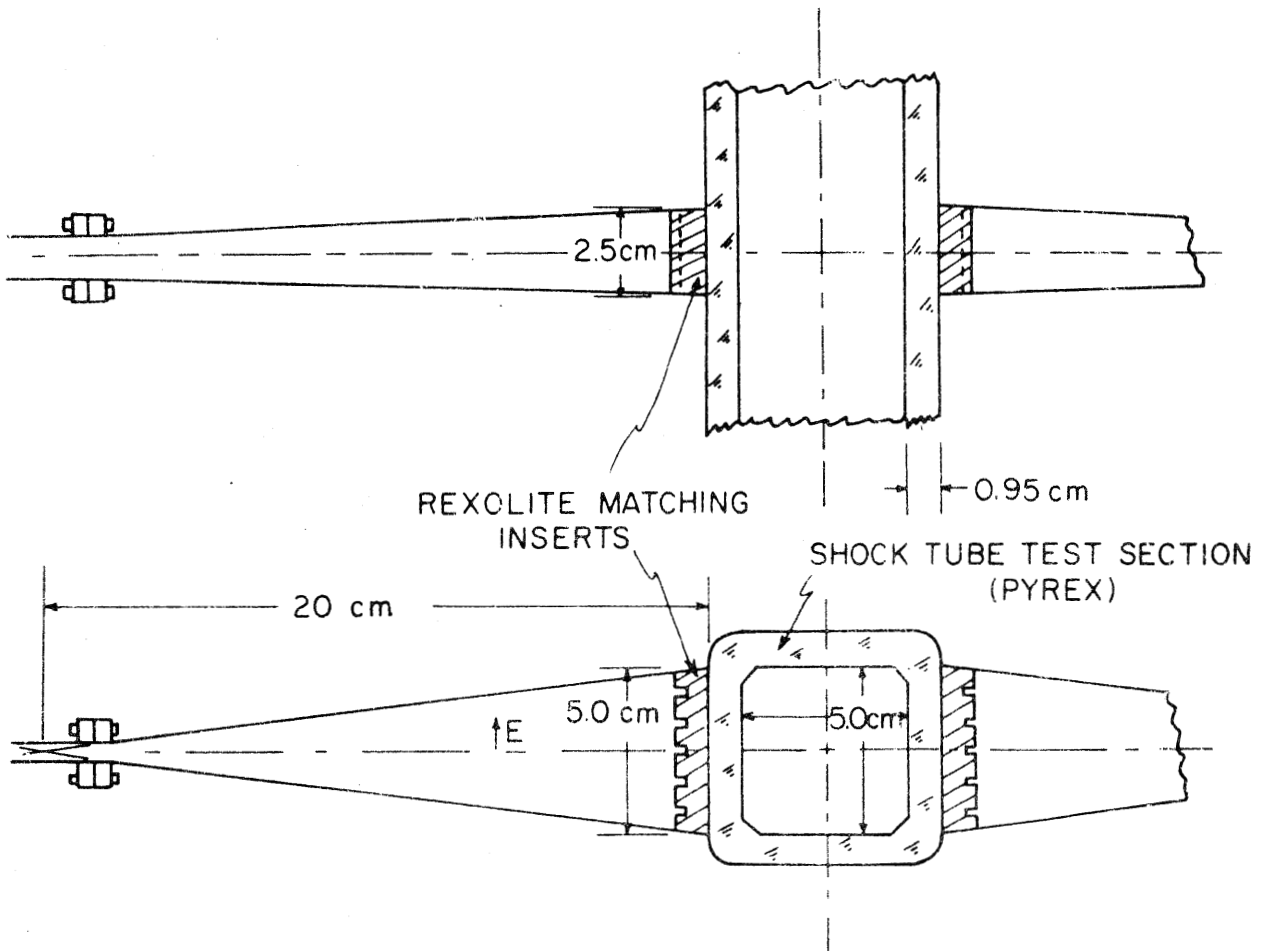


Fig. 7 Microwave Horn Assembly on Test Section

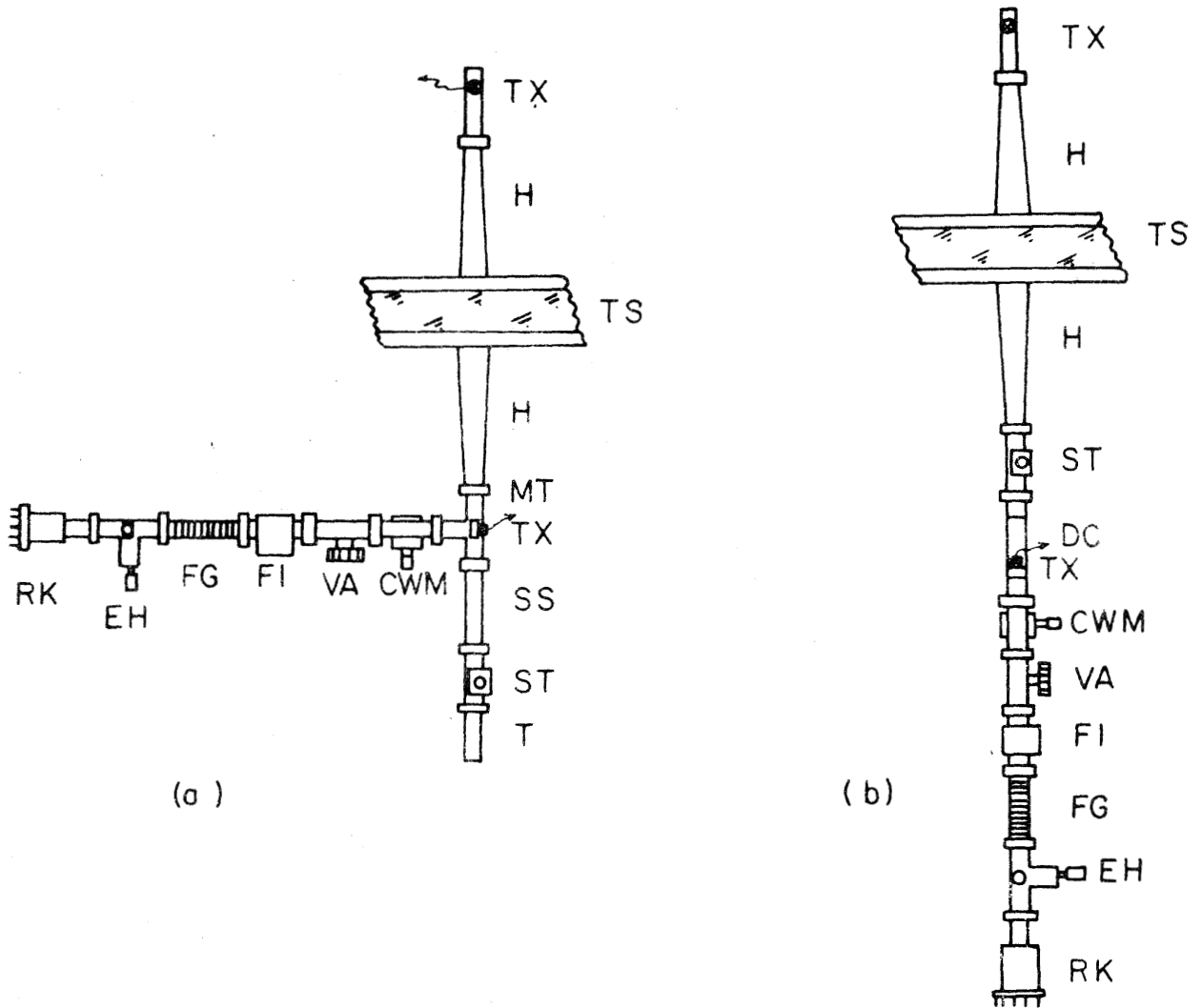
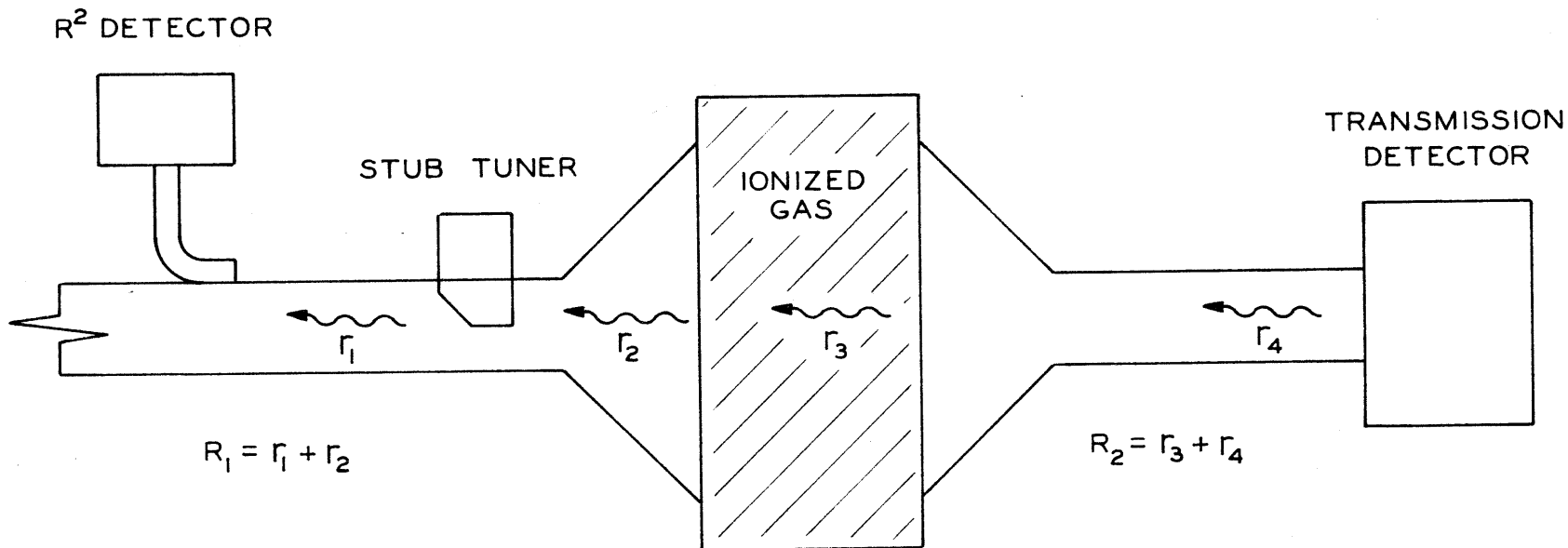


Fig. 8 Two Microwave Circuits for Ionized Gas Diagnostics: (a) Reflection Detector on Magic Tee; (b) Reflection Detector on Directional Coupler. Notation: RK, Reflex Klystron; EH, E and H Plane Tuner; FG, Section of Flexible Waveguide; FI, Ferrite Isolator; VA, Variable Attenuator; CWM, Cavity Wave Meter (absorption type); T, Termination; ST, Stub Tuner; SS, Straight Section; TX, Tunable Crystal Mount; H, Horn; MT, Magic Tee; DC, Directional Coupler; TS, Test Section (dielectric).



52

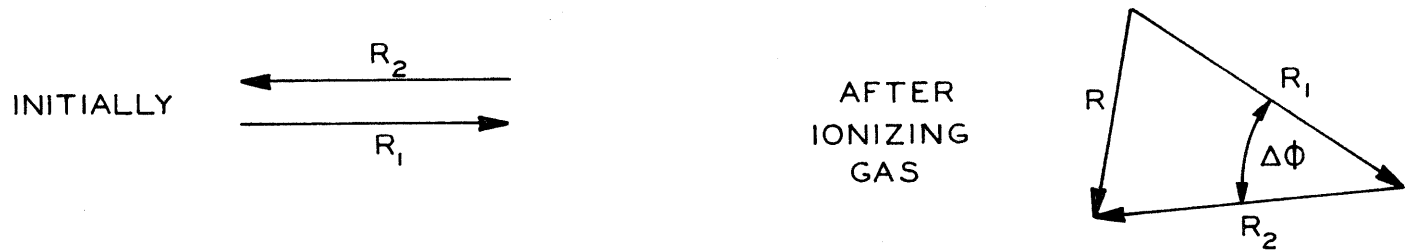


FIGURE 9 INTERFERENCE BUMPS IN R^2

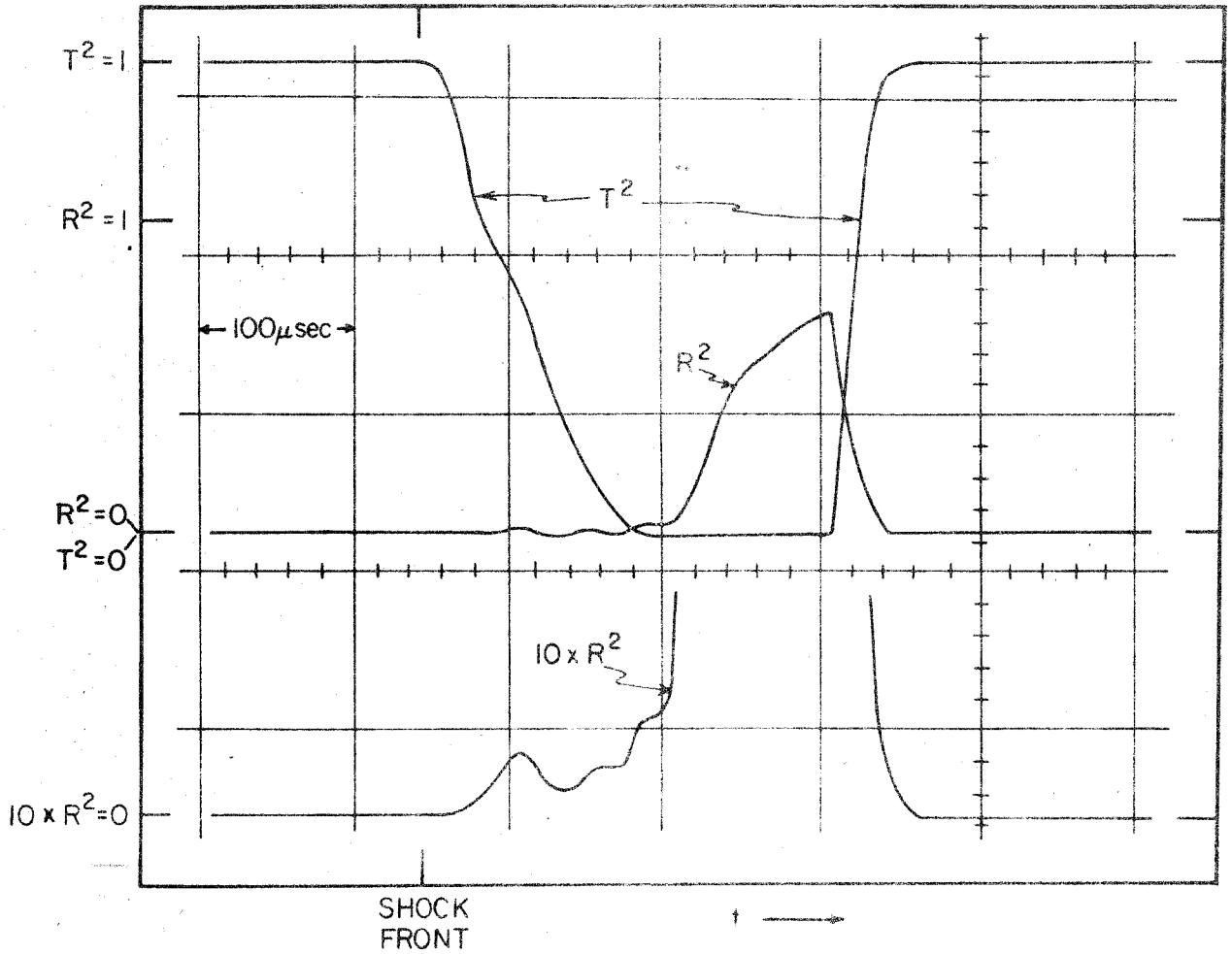


Fig. 10 Response of Transmission and Reflection Detectors to Passage of Mach 9 Shock Wave in Argon (Initial Pressure 5 mm).

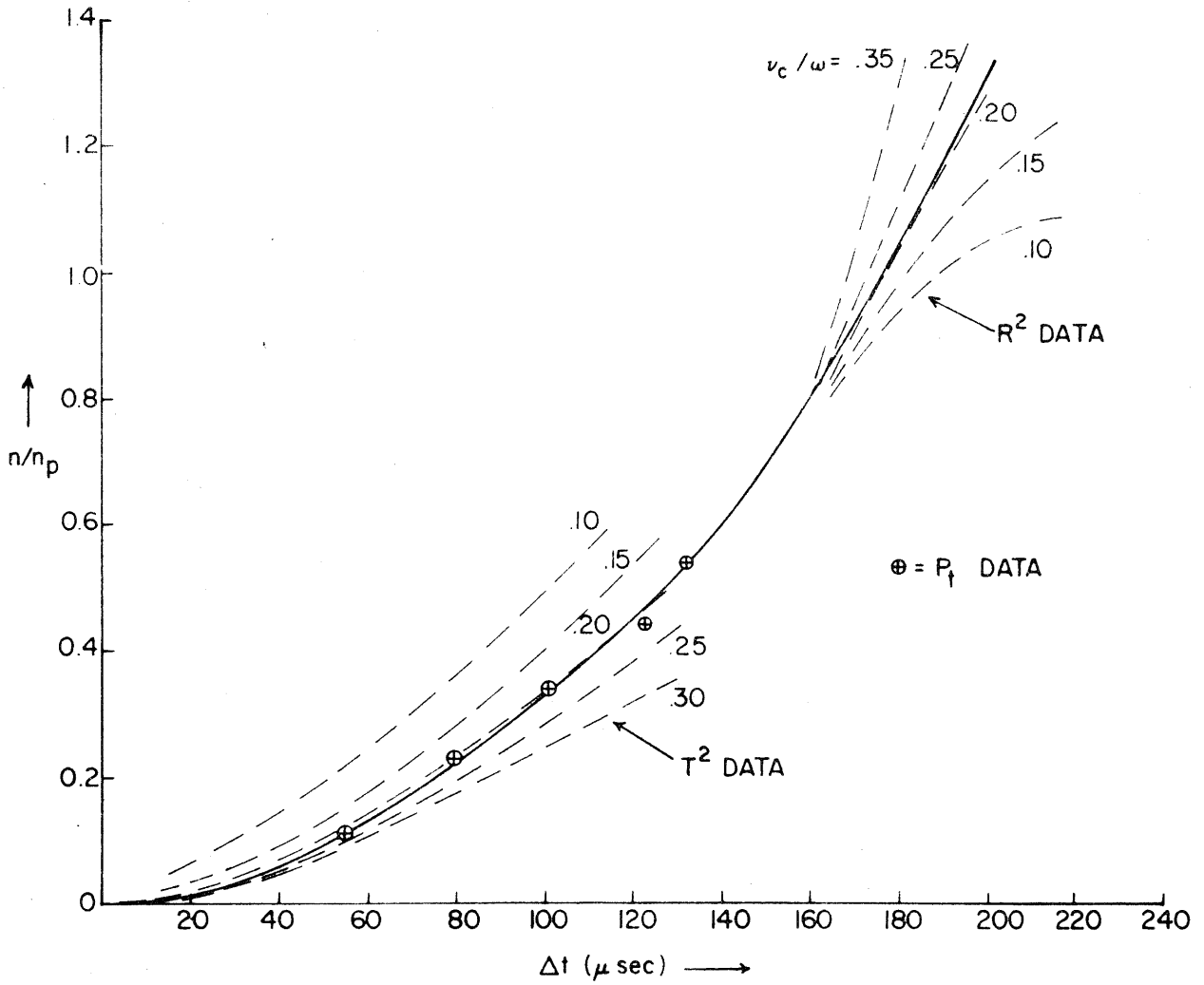


Fig. 11' Construction of Composite $n(t)$ Curve by Identification of Effective Collision Frequency (see text).

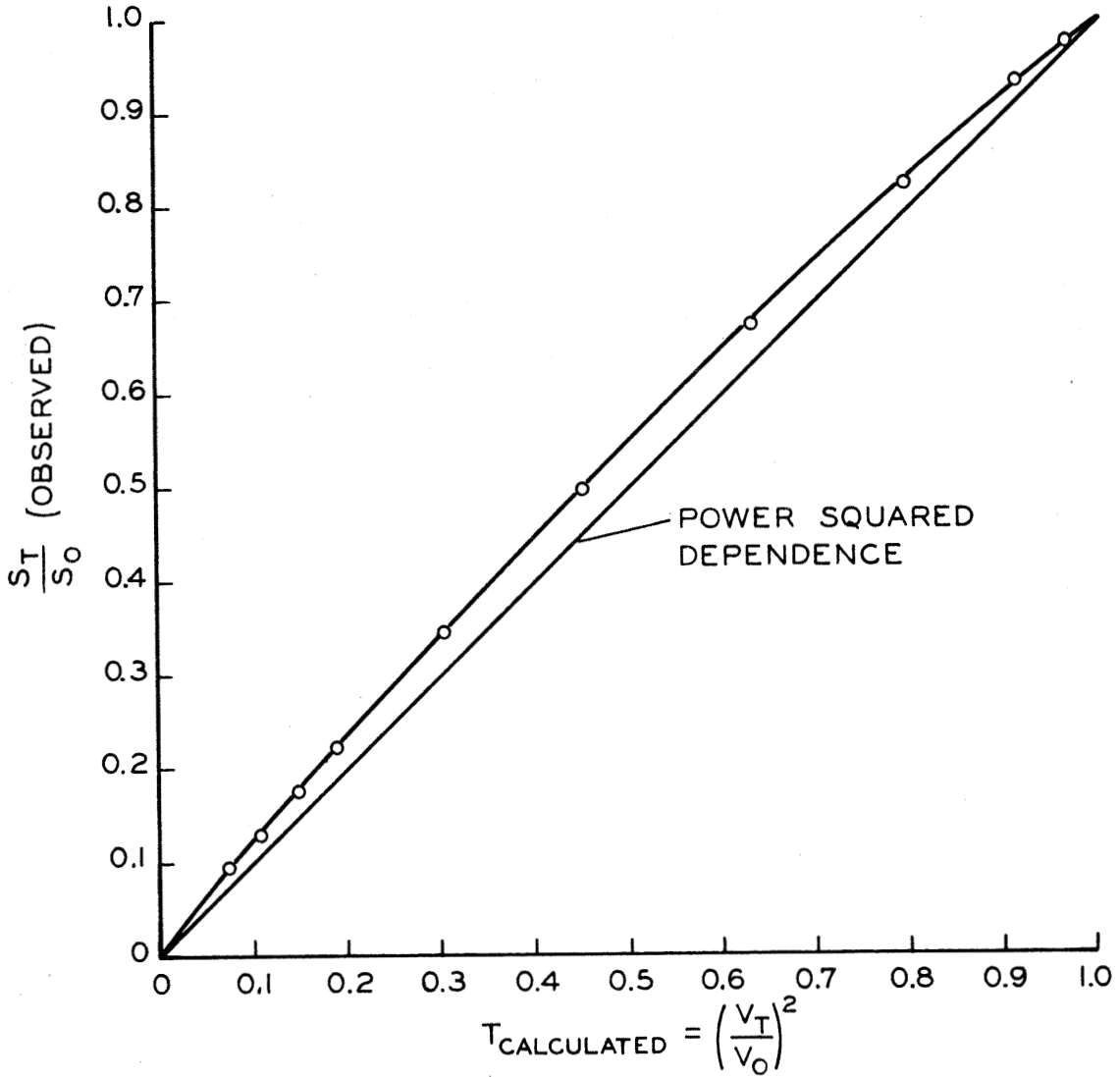


FIGURE 12 IN26 TRANSMISSION CRYSTAL CALIBRATION CURVE

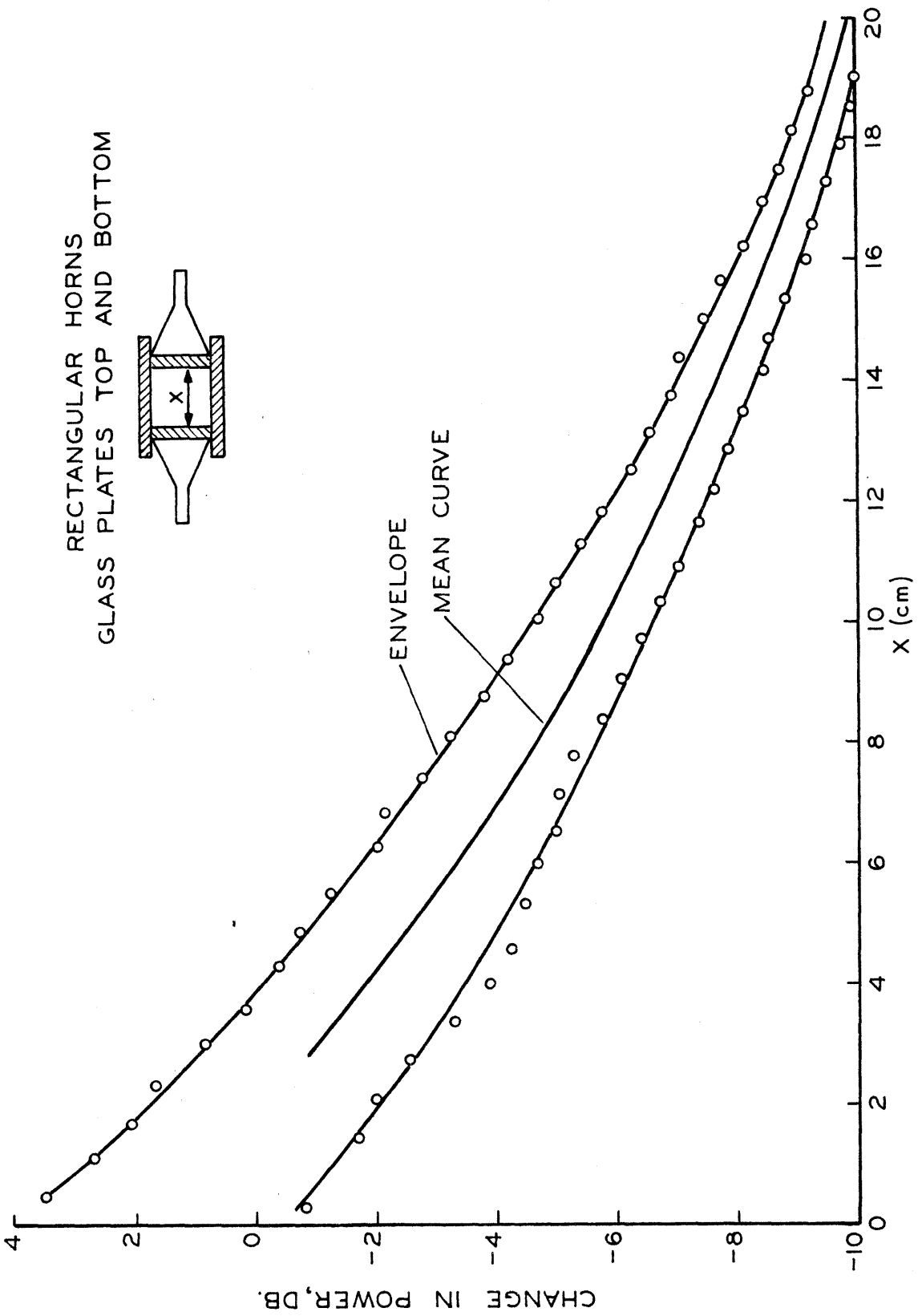


FIGURE 13 HORN POWER VERSUS HORN SEPARATION

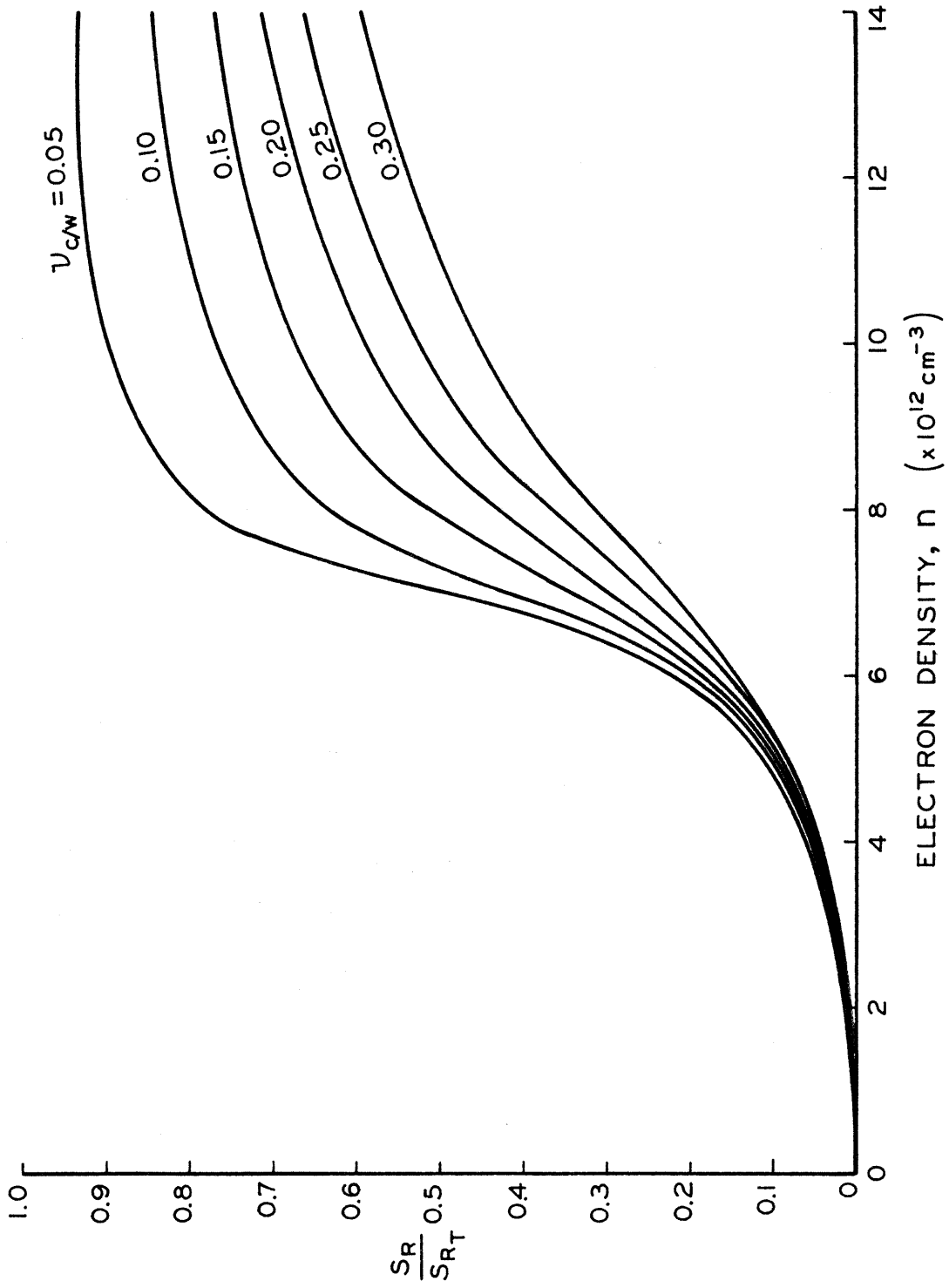


FIGURE 15 CORRECTED REFLECTED SIGNAL

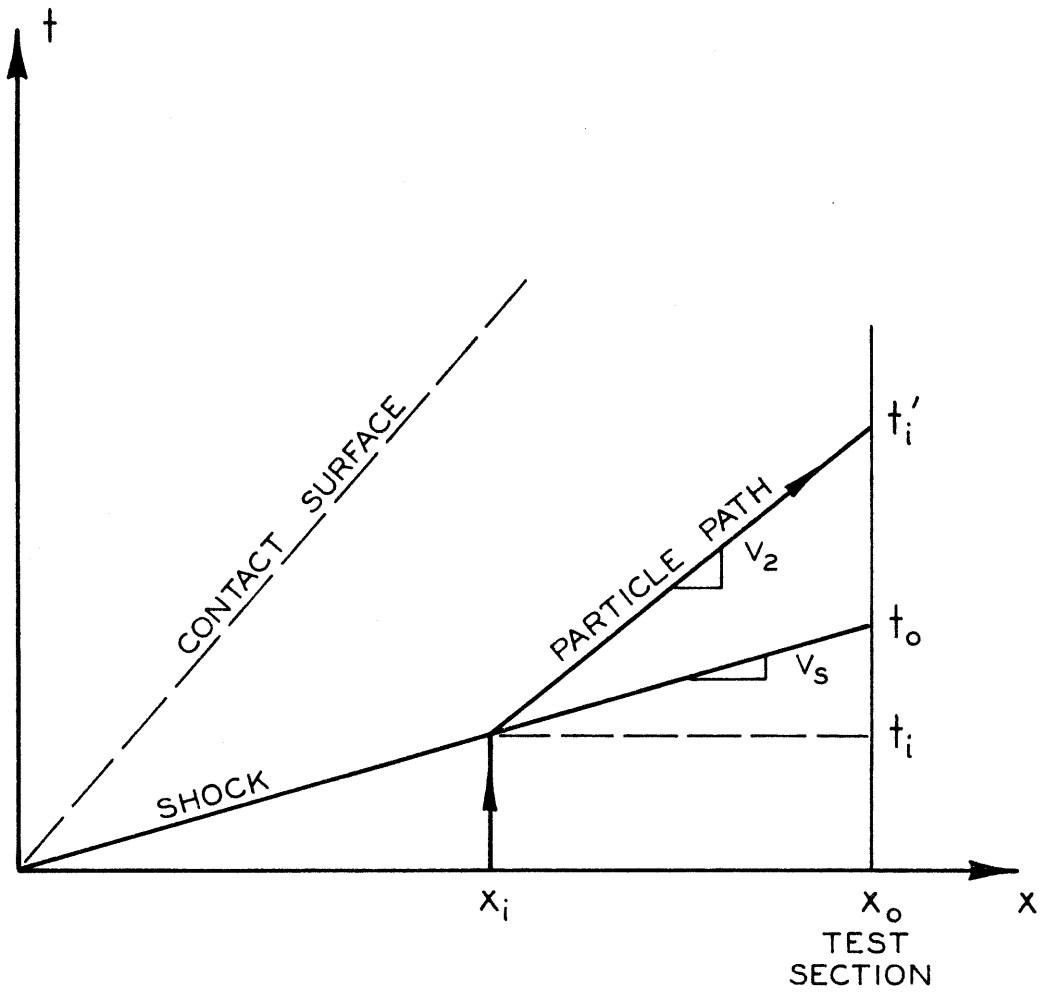


FIGURE 16 $x - t$ DIAGRAM FOR SIMPLE TUBE

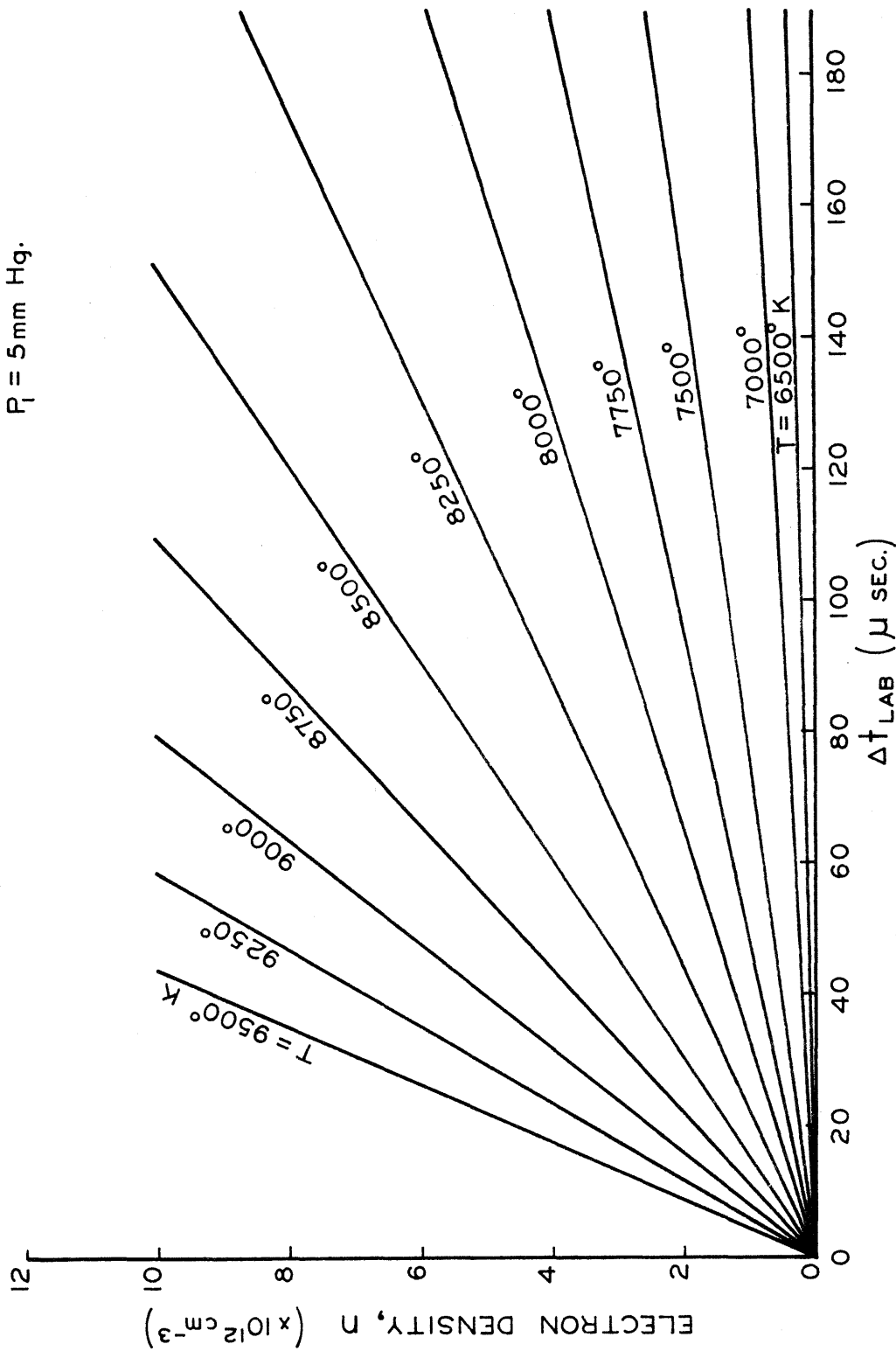


FIGURE 17 ELECTRON DENSITY GROWTH BEHIND SHOCK WAVE IN ARGON

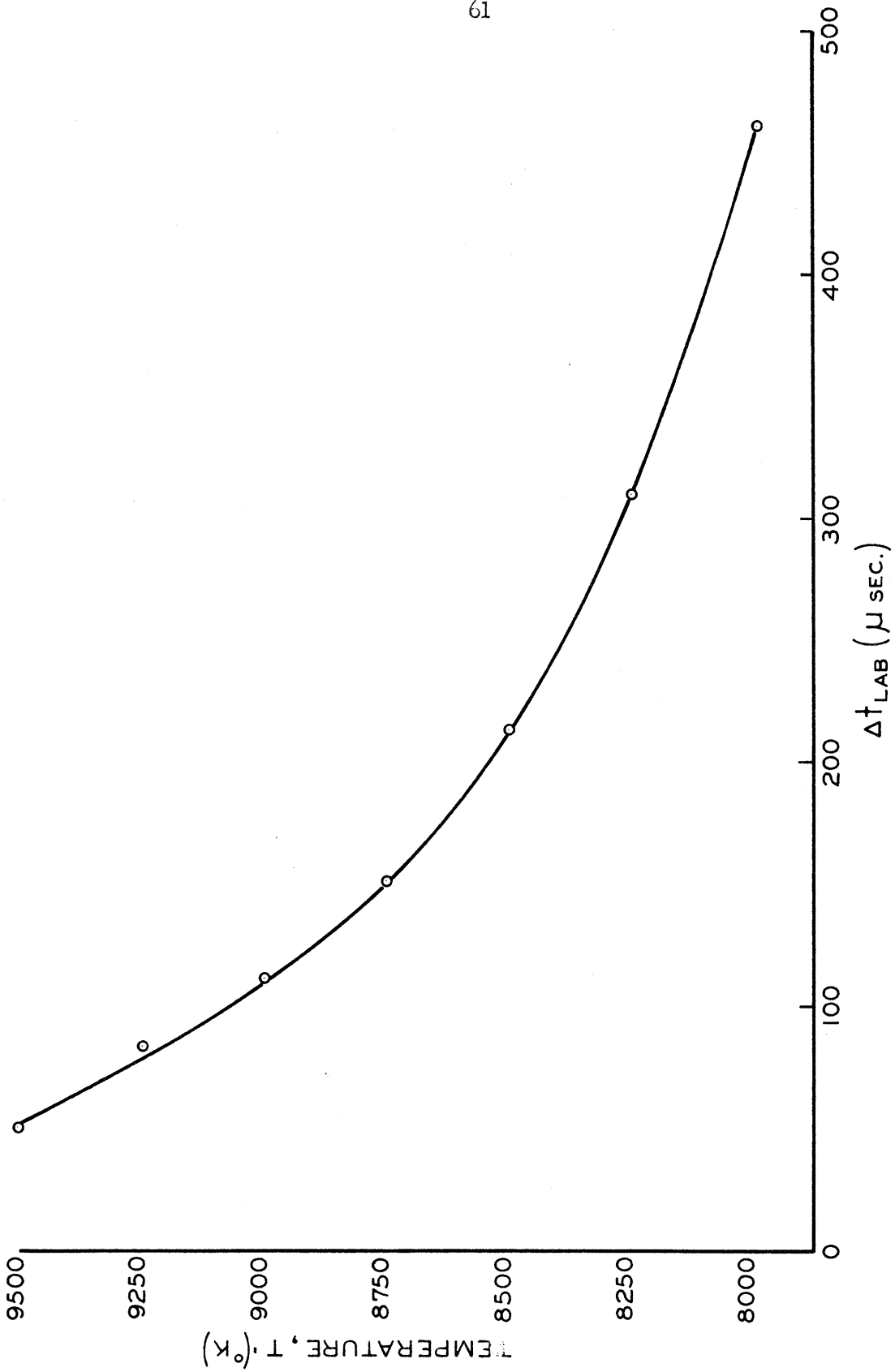


FIGURE 18 TIME REQUIRED TO REACH e-A PROCESS IN ARGON ($\dot{n}_e \approx 1.4 \times 10^{16} \text{ cm}^{-3} \text{ sec}^{-1}$)

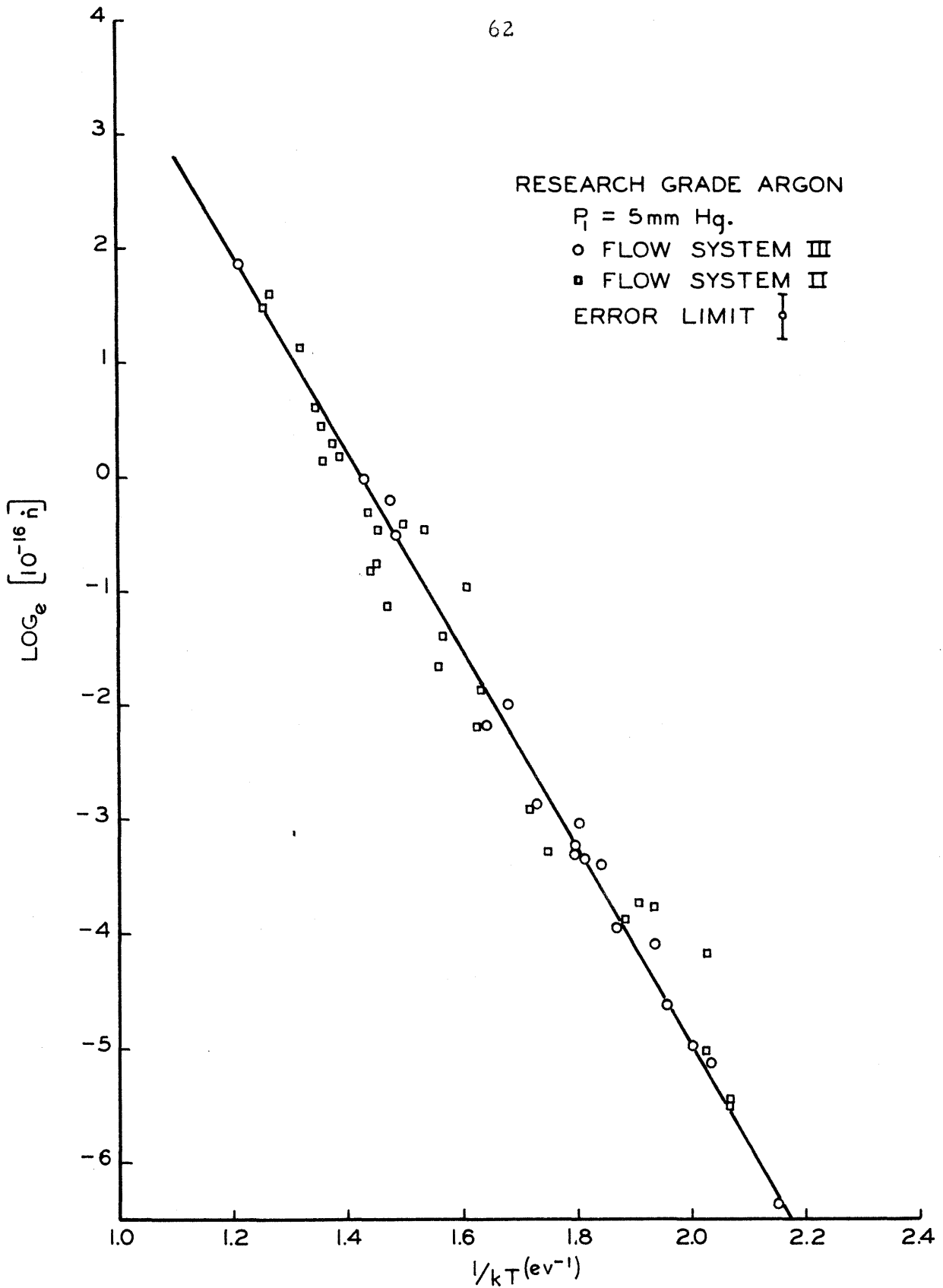


FIGURE 19 RATE OF IONIZATION IN ARGON

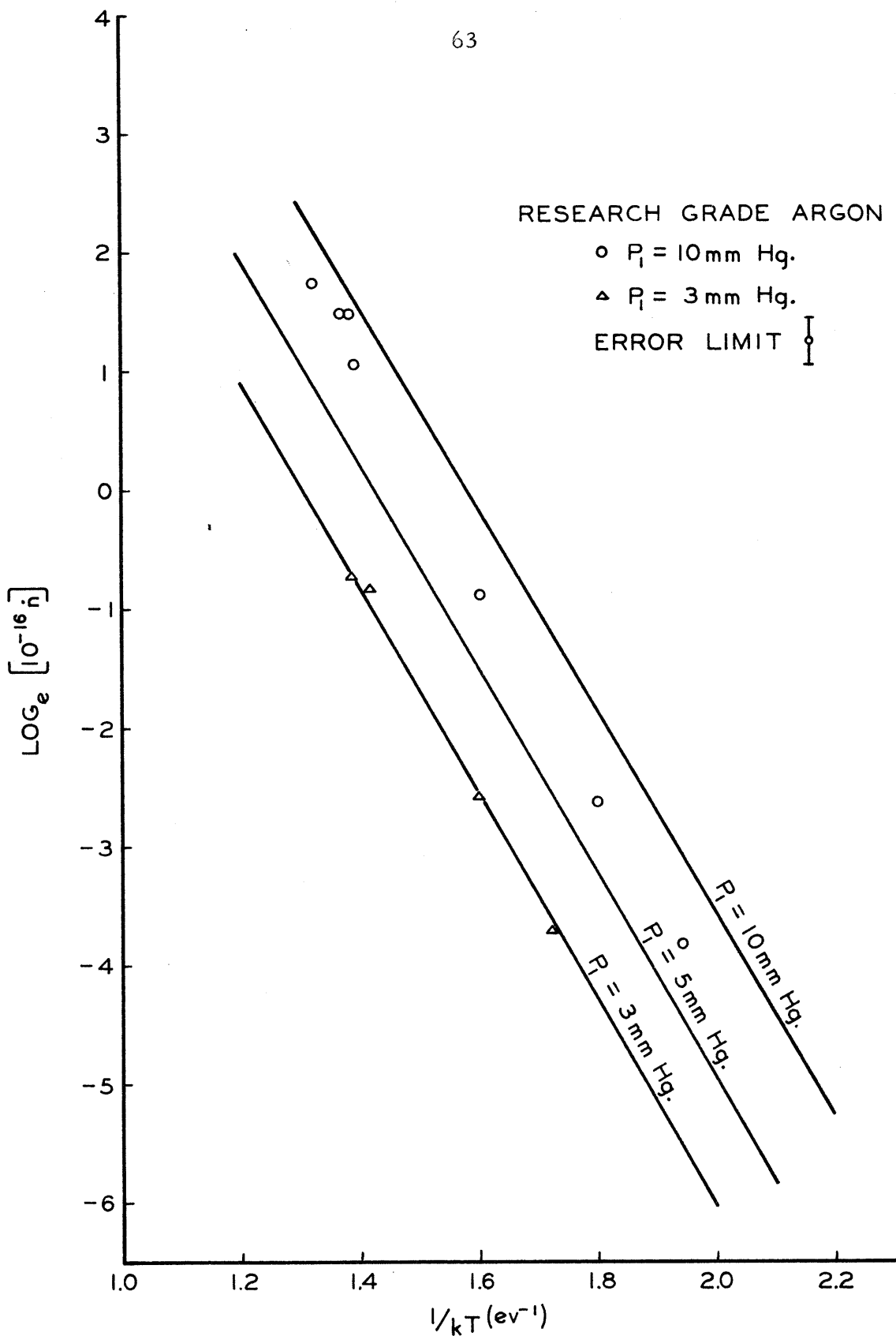


FIGURE 20 EFFECT OF CHANGING INITIAL PRESSURE

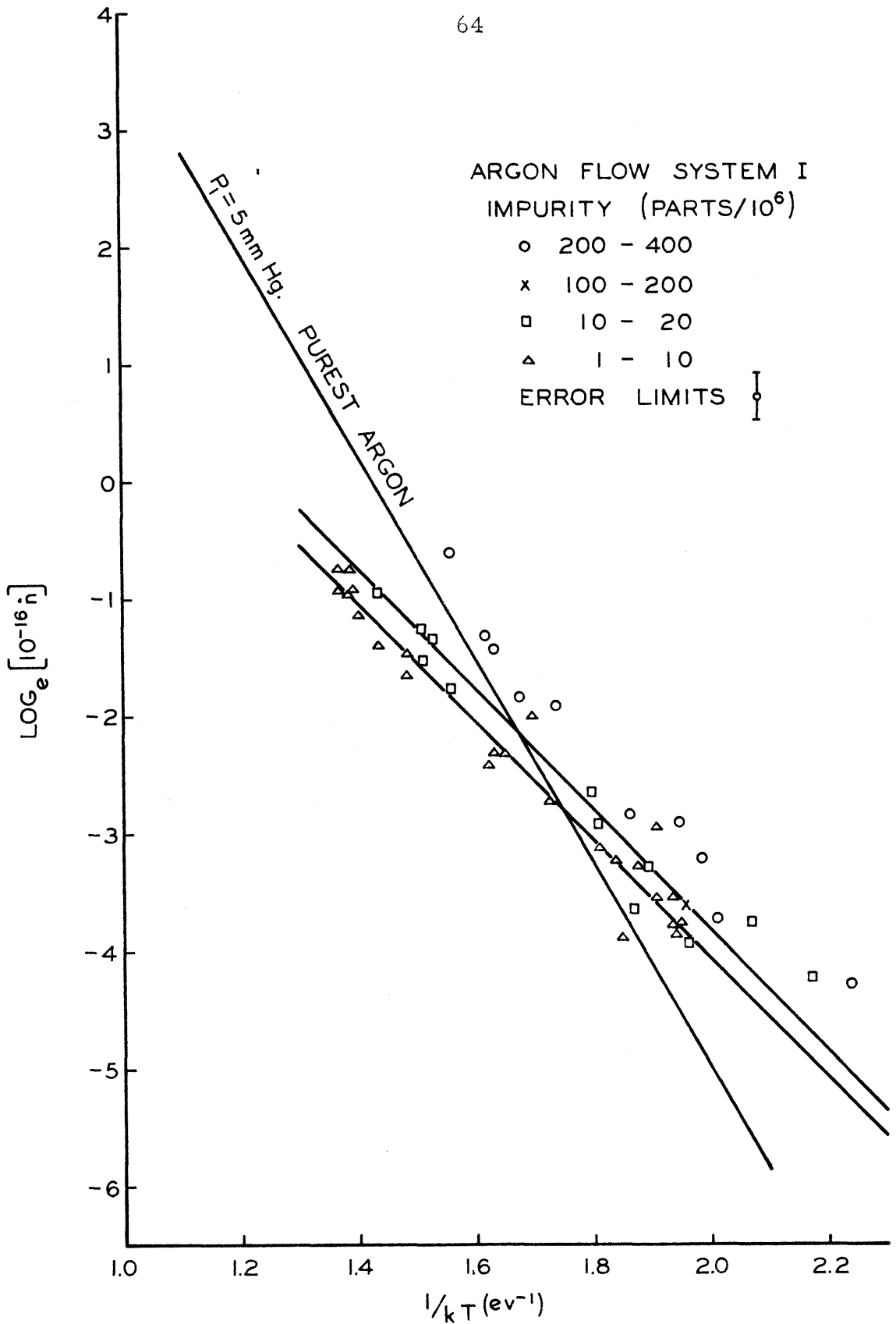


FIGURE 21 EFFECT OF PURITY ON ARGON IONIZATION

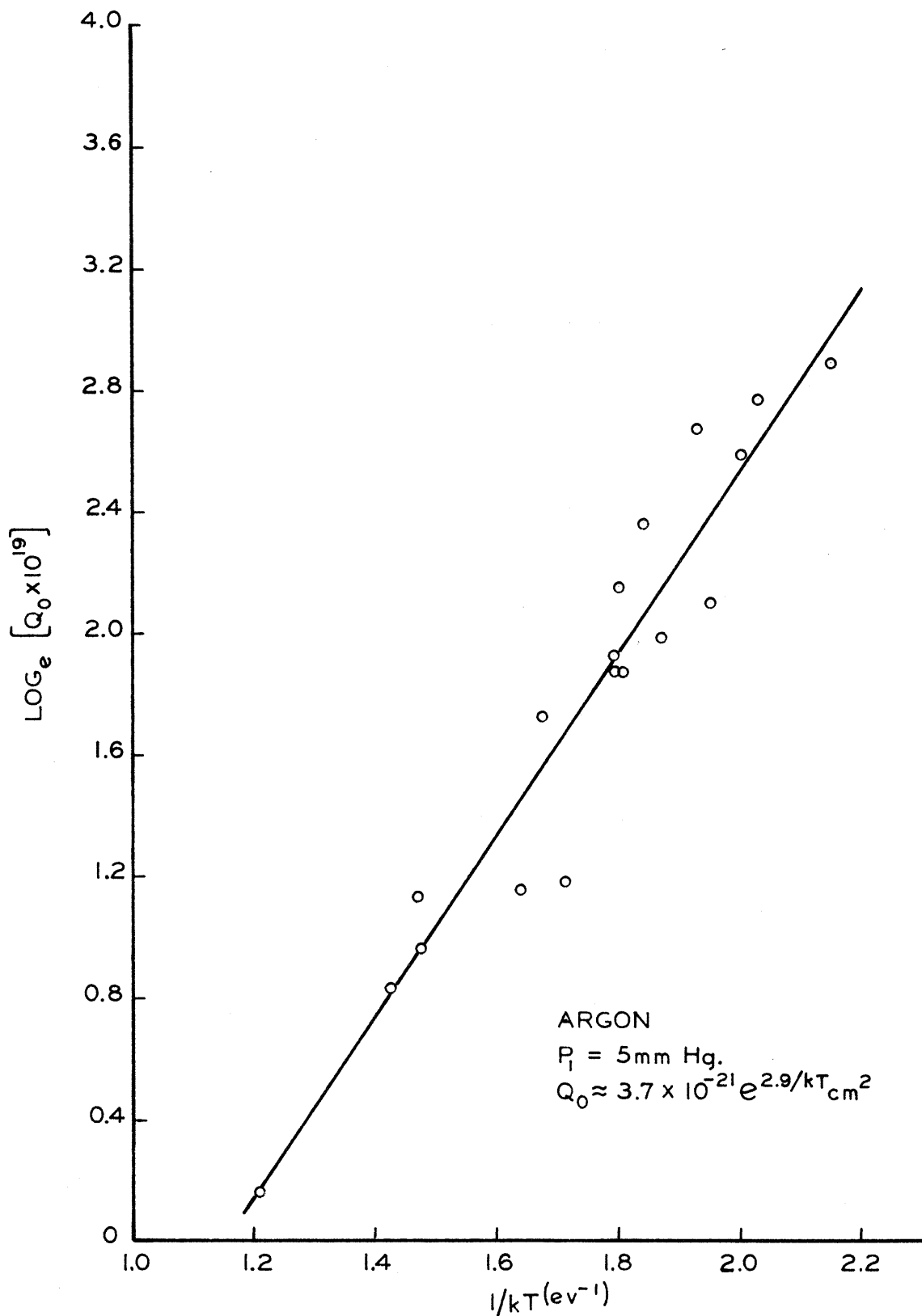


FIGURE 22 CROSS SECTION DEFINED BY WEYMANN

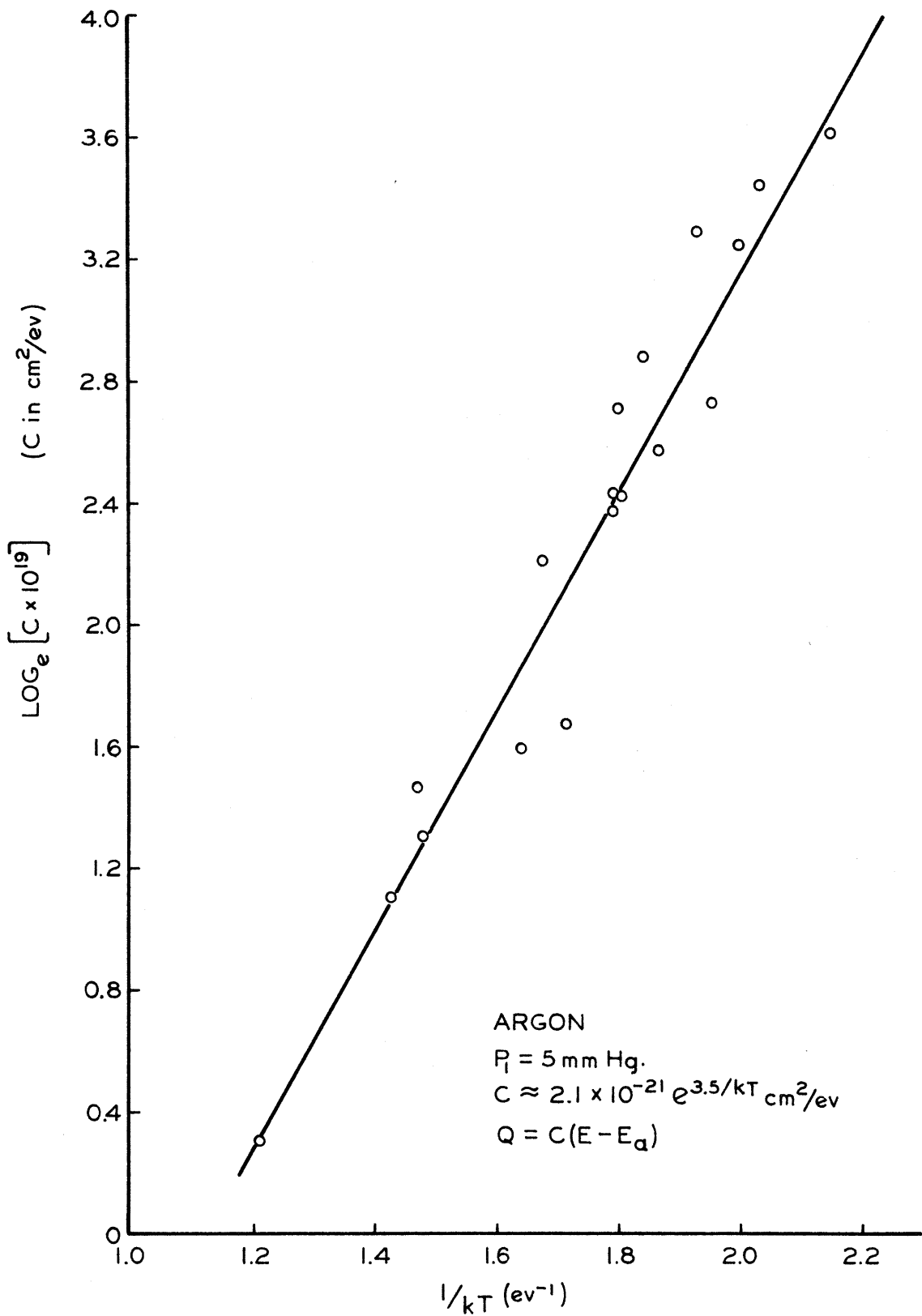


FIGURE 23 CROSS-SECTION PARAMETER C

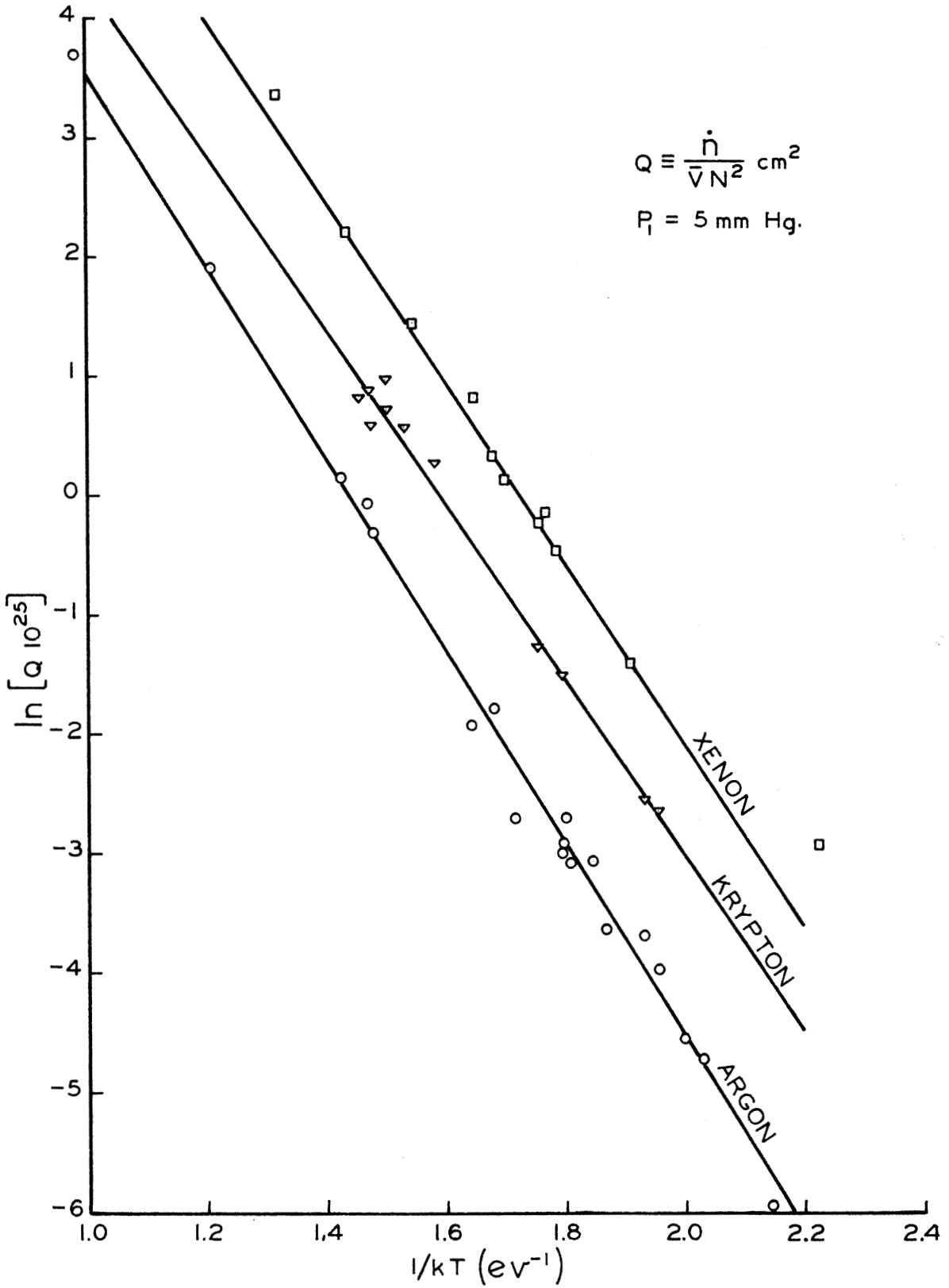


FIGURE 24 IONIZATION CROSS-SECTION Q FOR ARGON, KRYPTON AND XENON

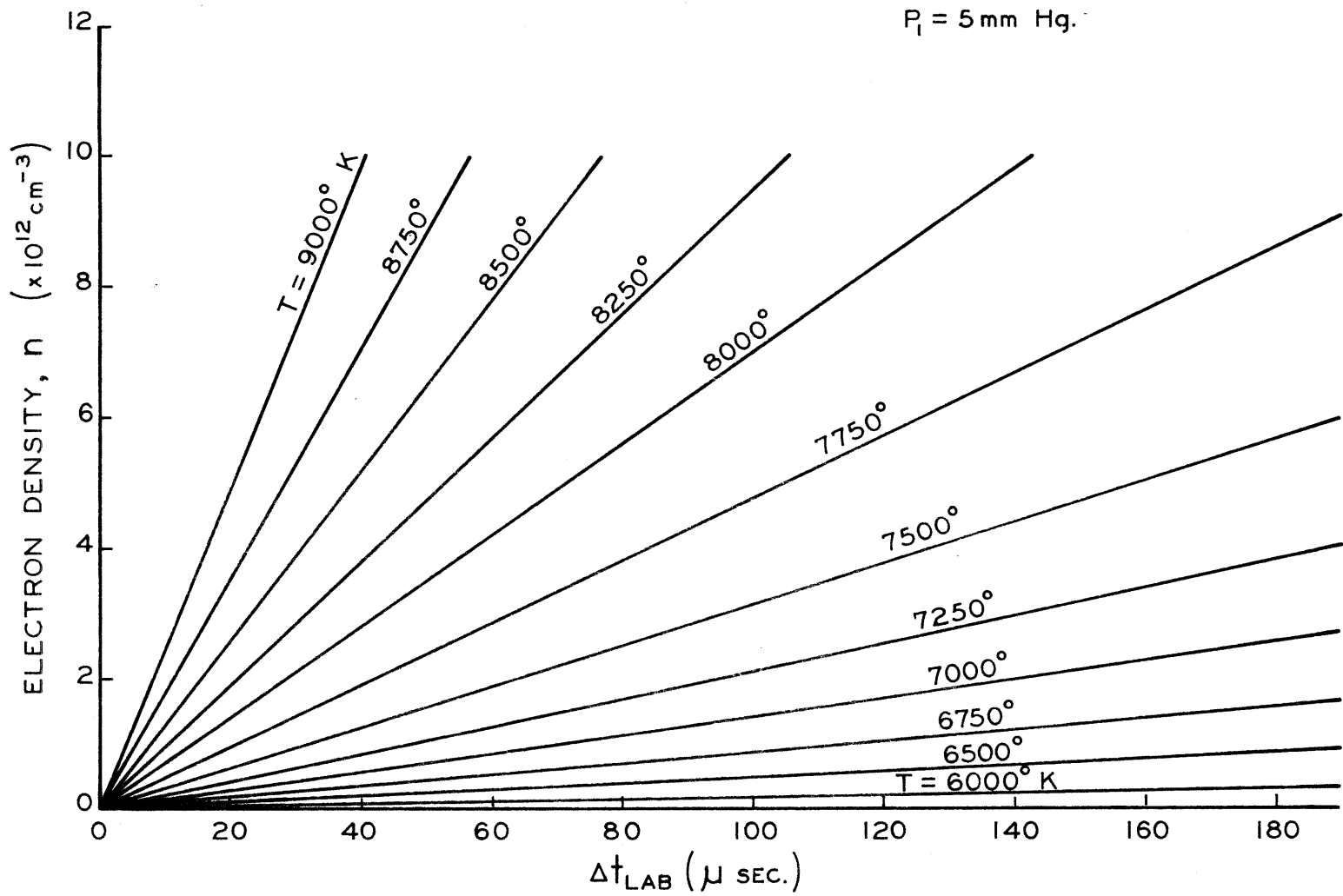


FIGURE 25 ELECTRON DENSITY GROWTH BEHIND SHOCK WAVE IN KRYPTON

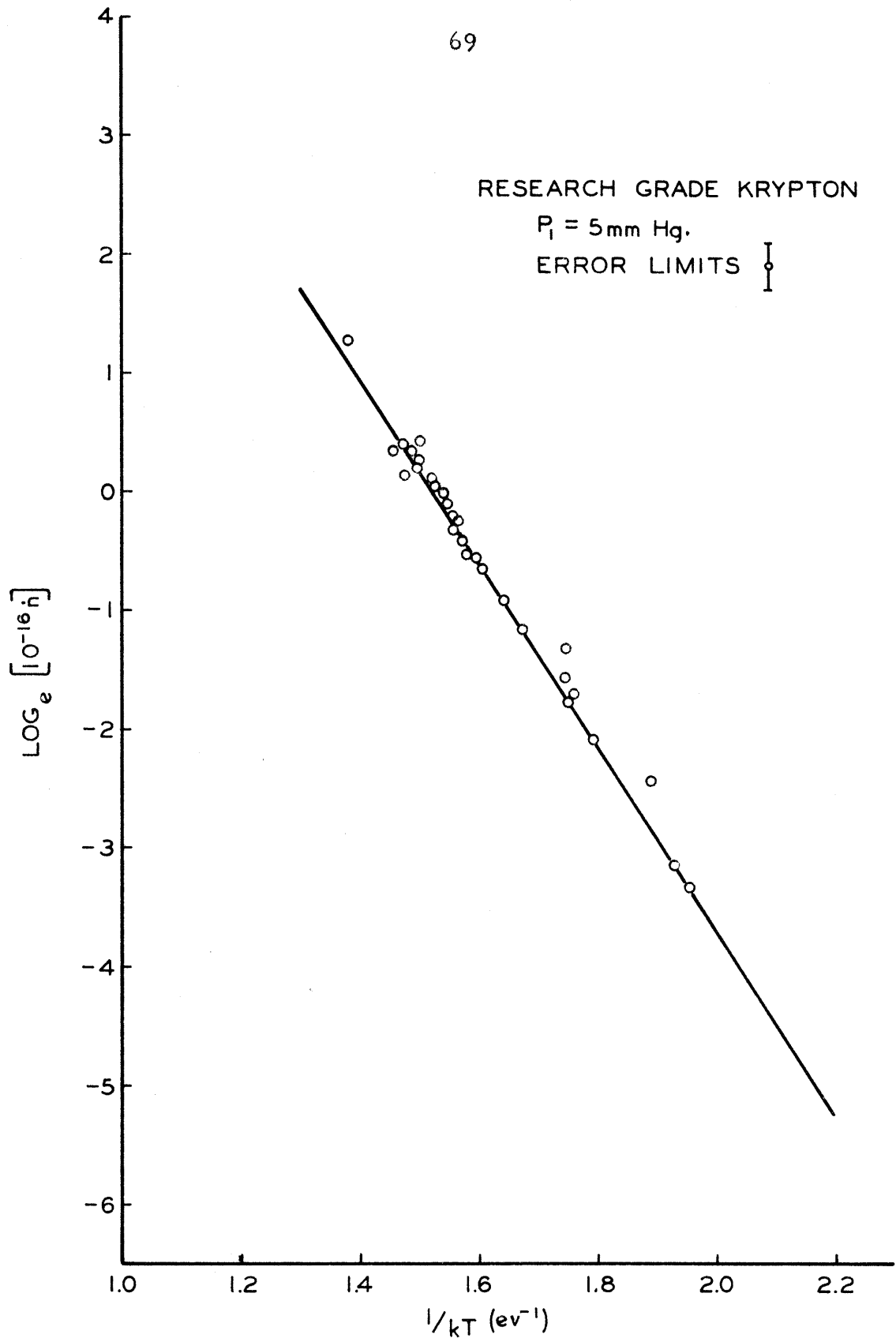


FIGURE 26 RATE OF IONIZATION OF RESEARCH GRADE KRYPTON

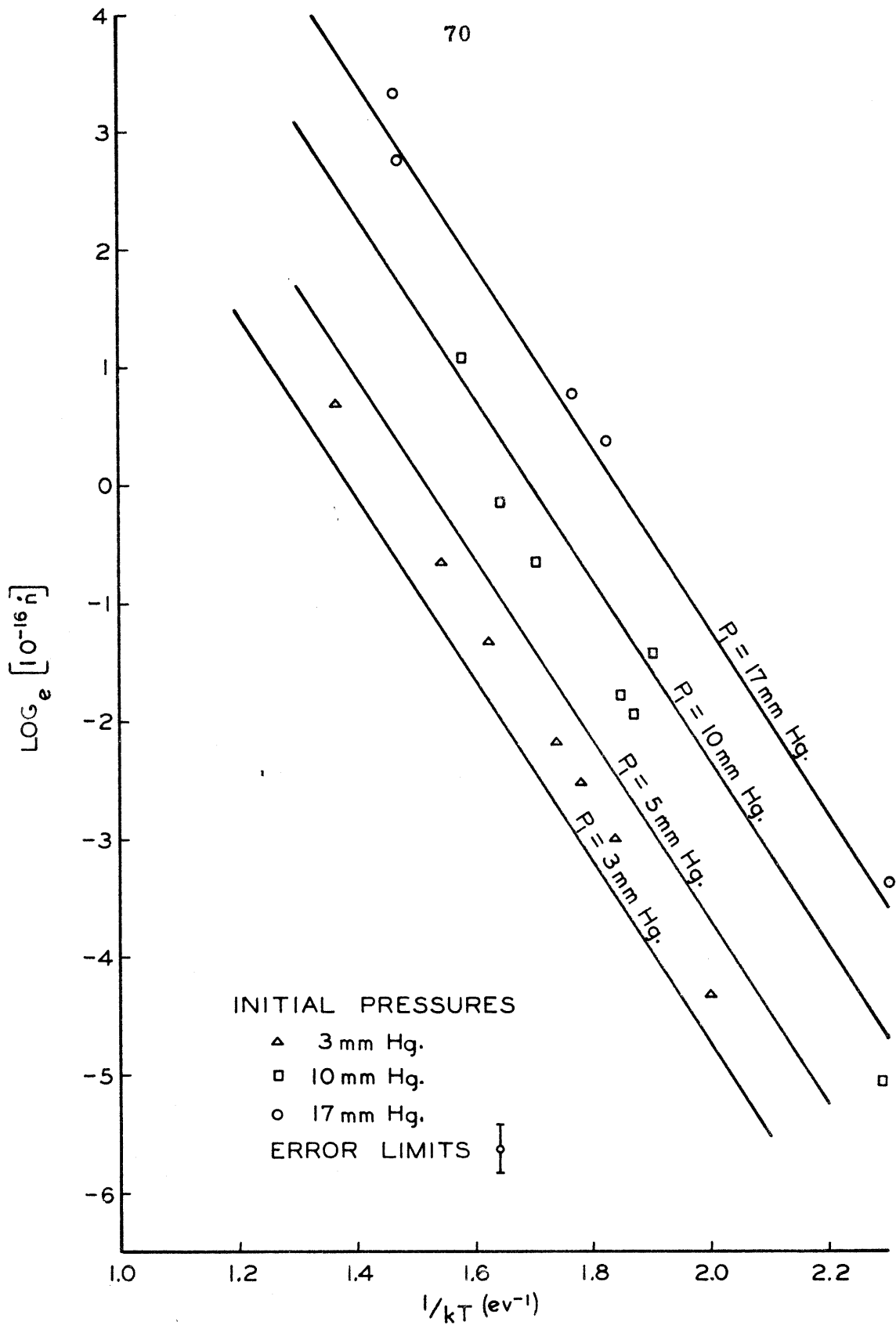


FIGURE 27 PRESSURE DEPENDENCE IN KRYPTON

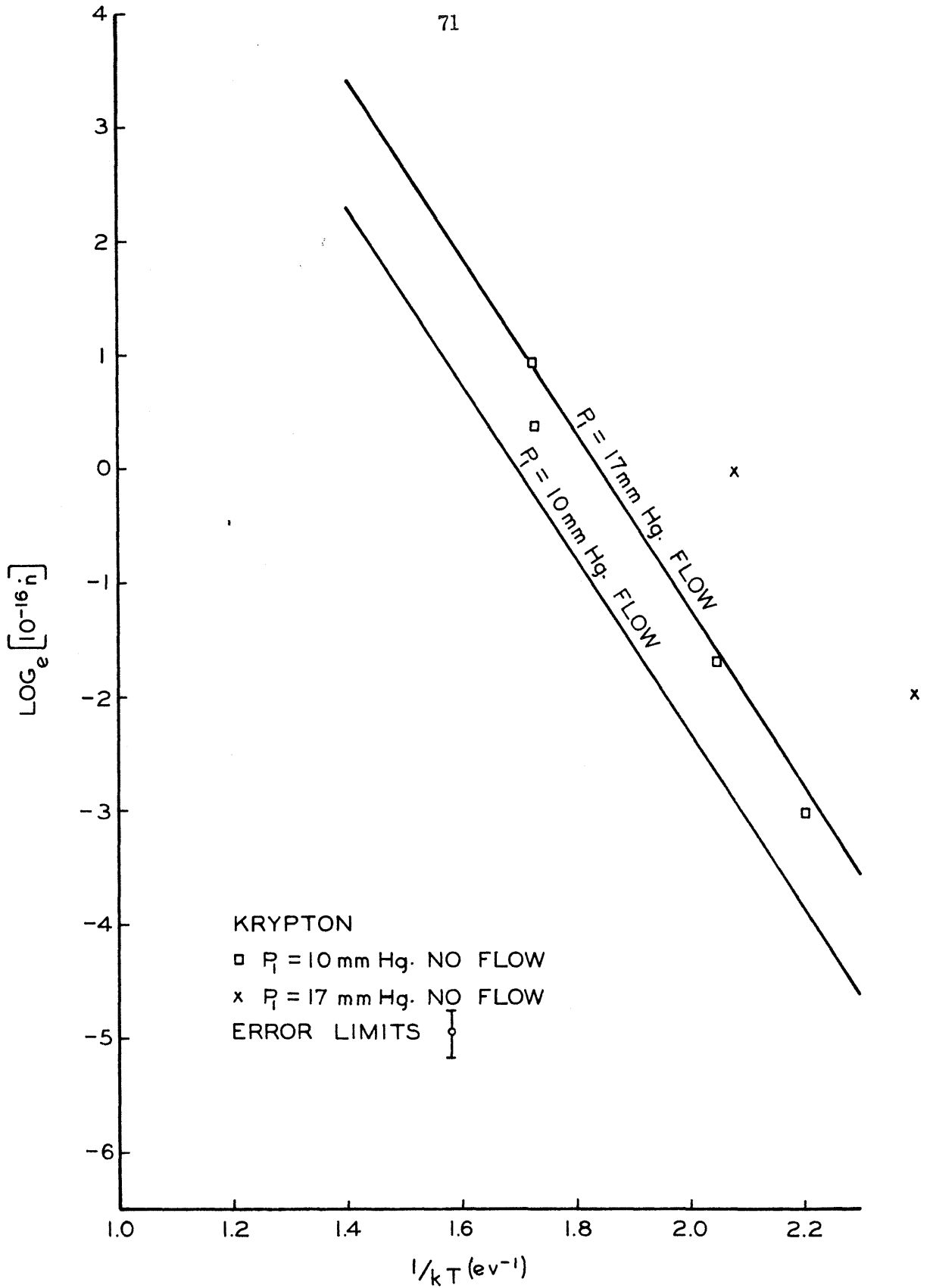


FIGURE 28 EFFECT OF FLOW SYSTEM

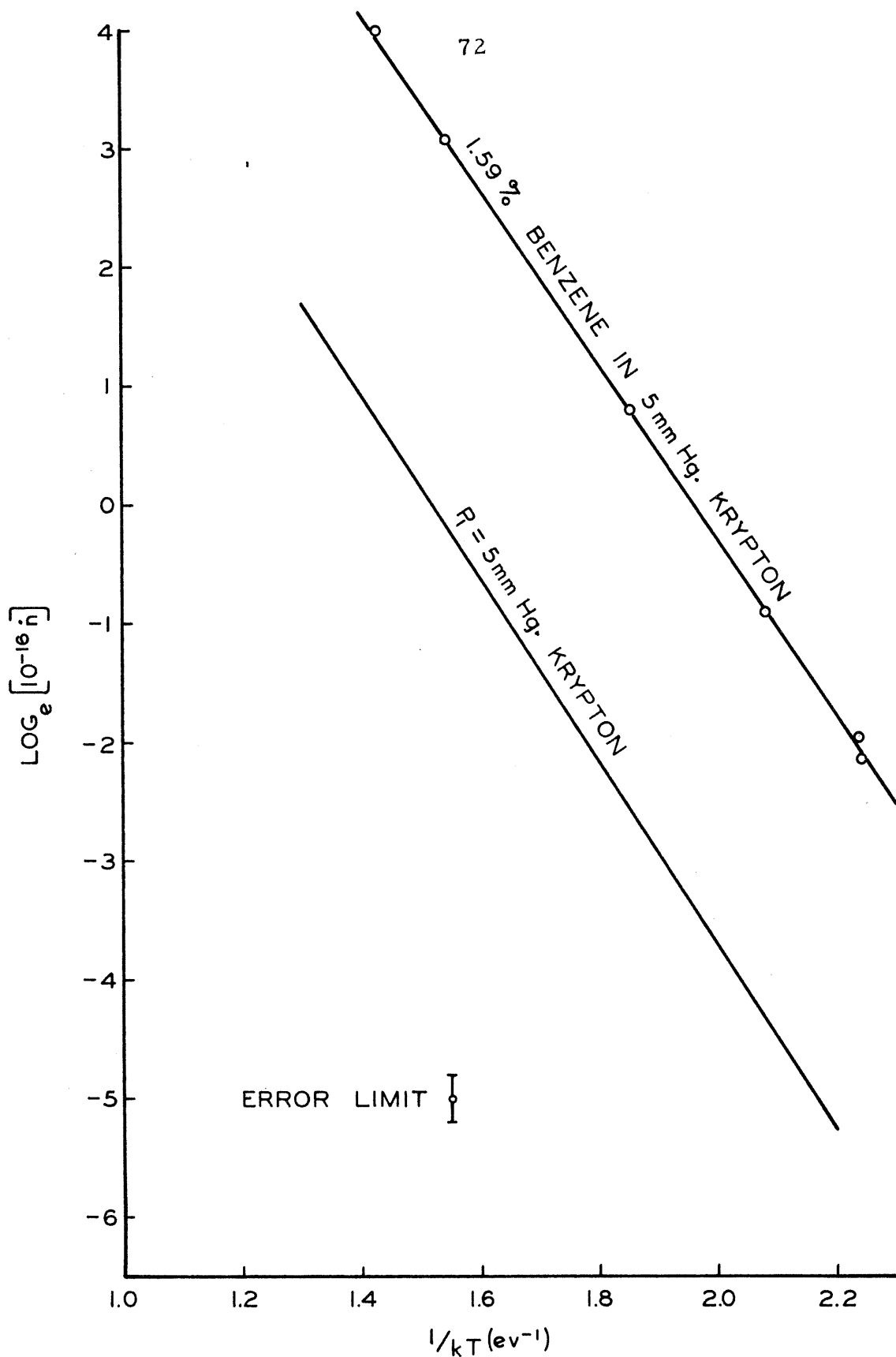


FIGURE 29 IMPURITY EFFECT OF BENZENE

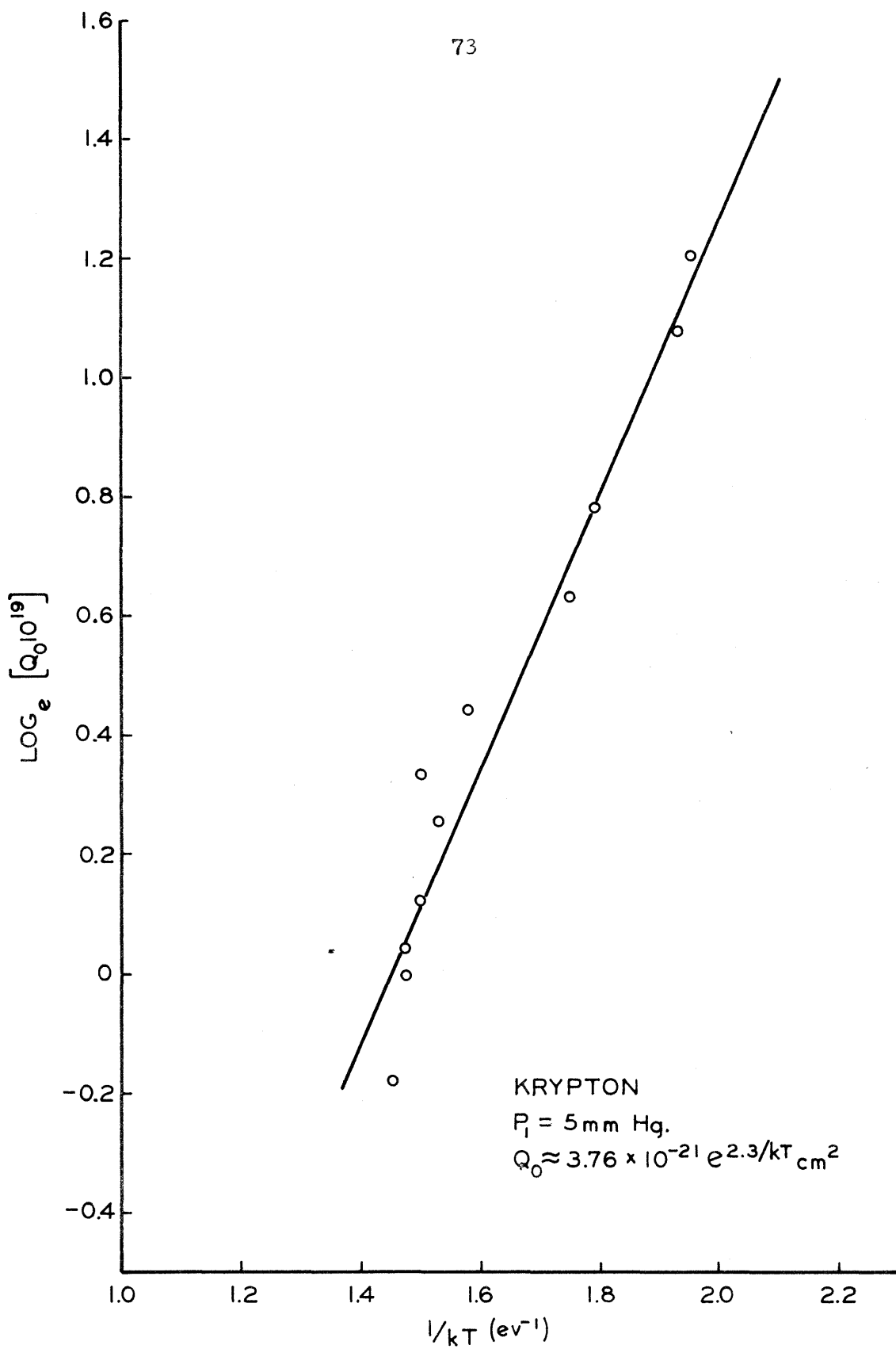


FIGURE 30 CROSS-SECTION DEFINED BY WEYMANN

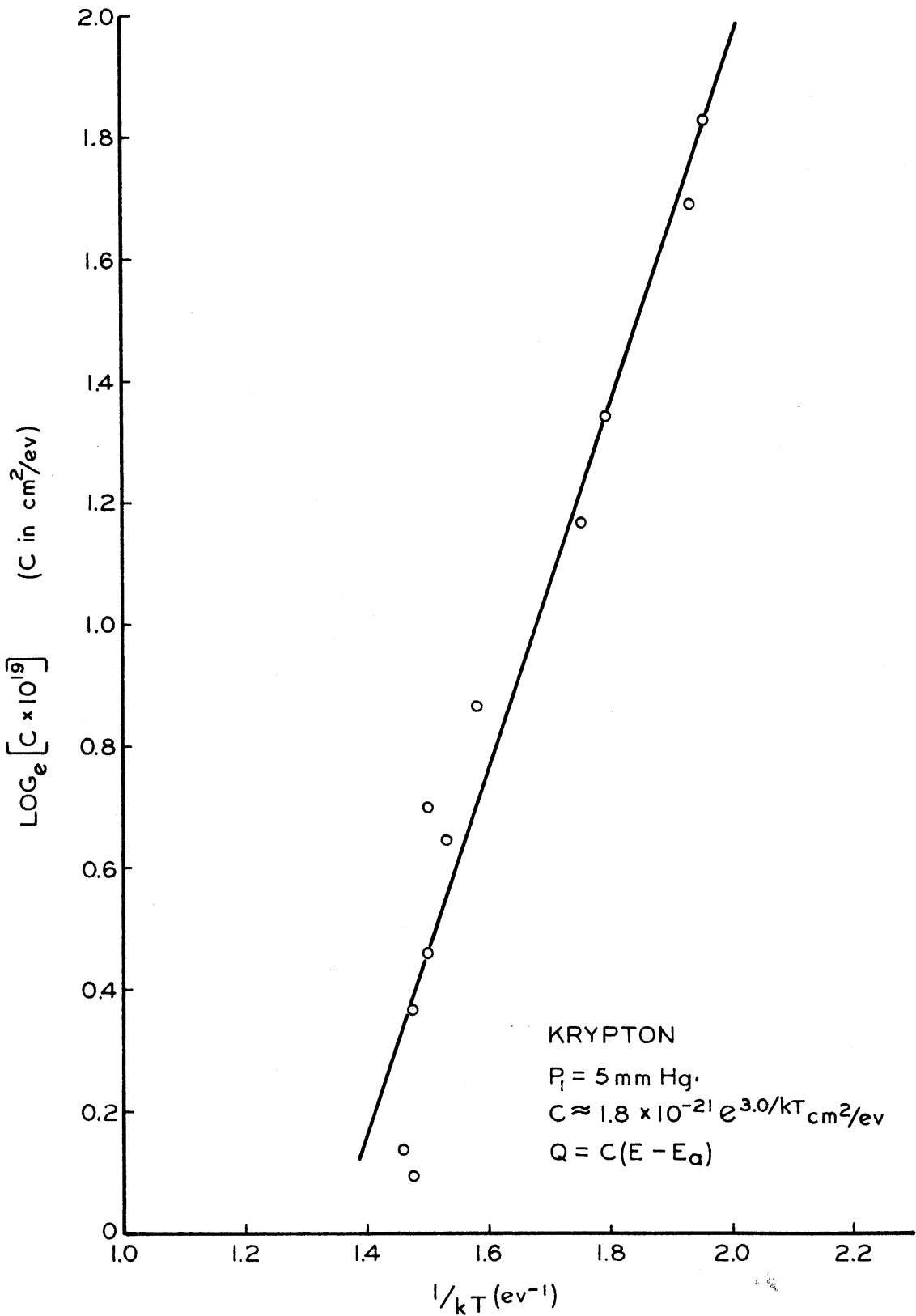


FIGURE 31 CROSS-SECTION PARAMETER C

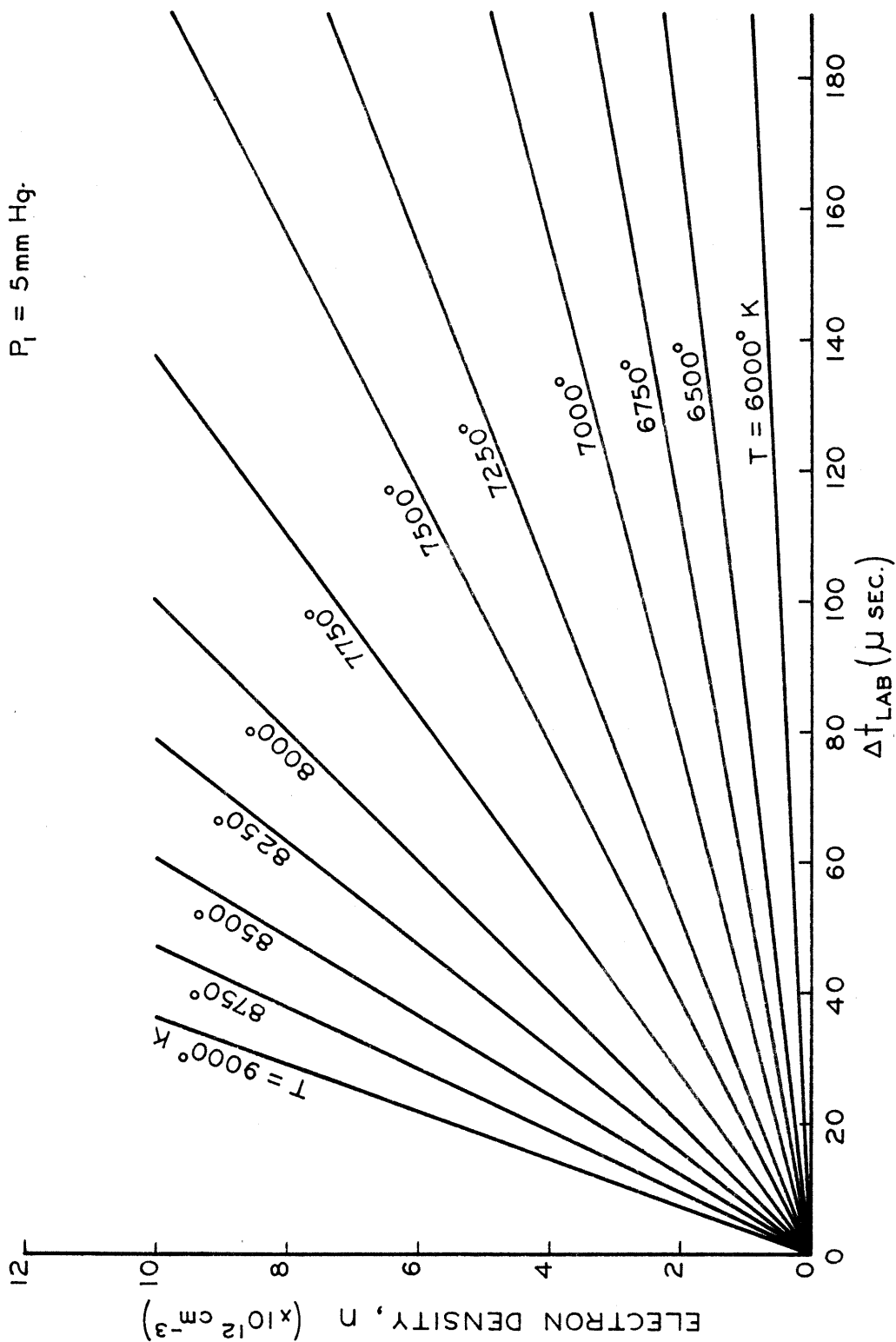


FIGURE 32 ELECTRON DENSITY GROWTH BEHIND SHOCK WAVES IN XENON

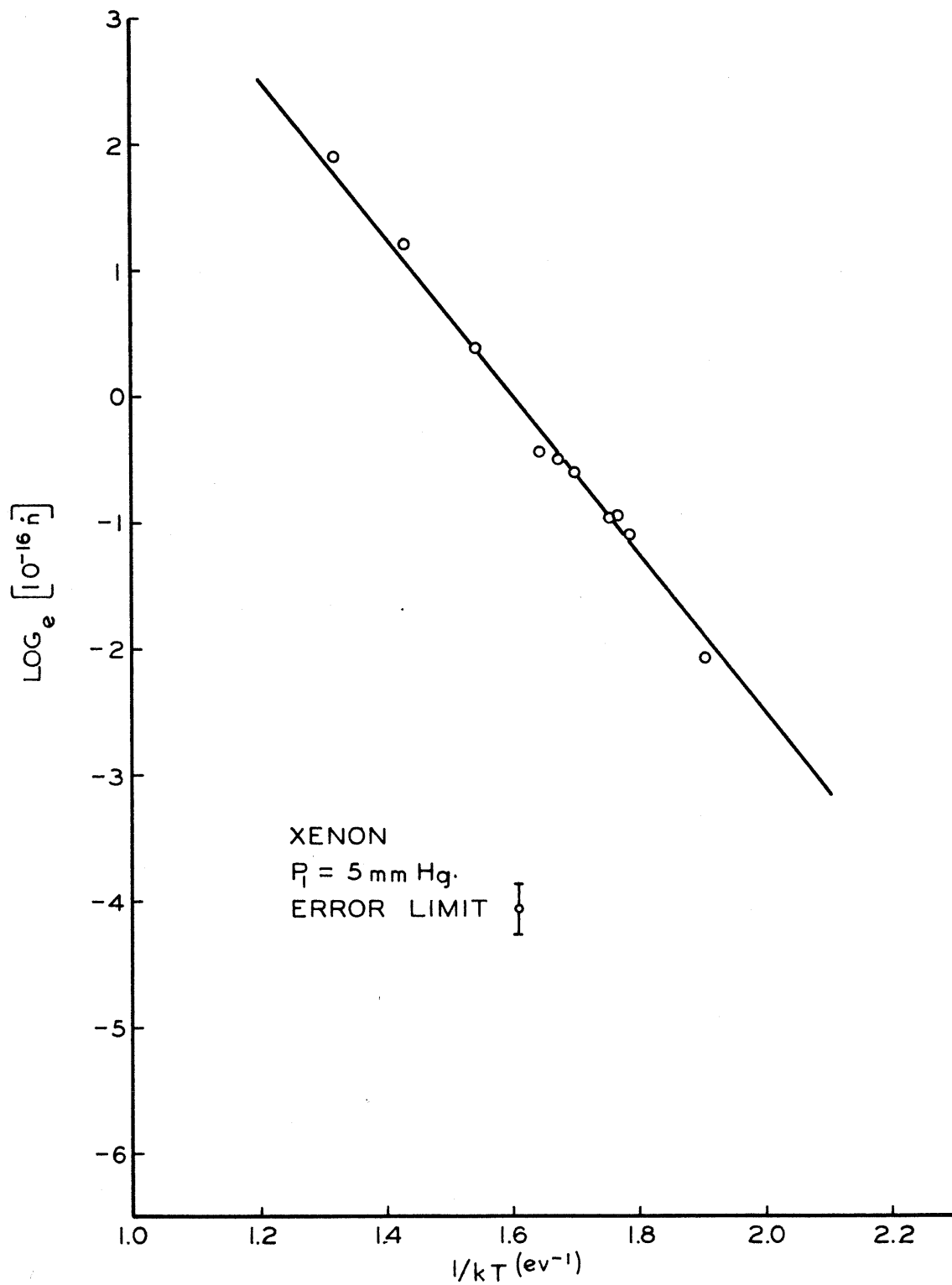


FIGURE 33 IONIZATION RATES IN XENON

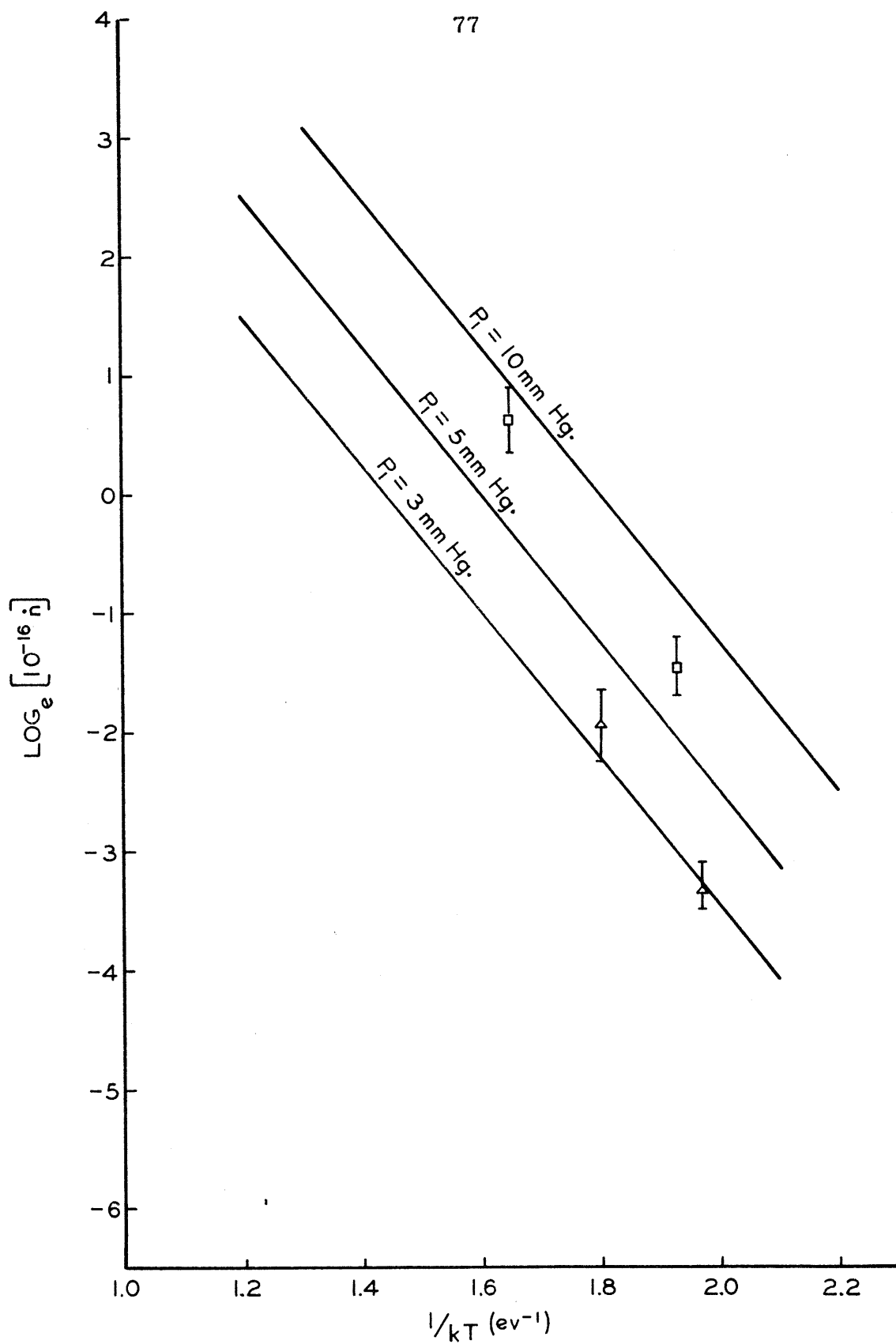


FIGURE 34 PRESSURE DEPENDENCE IN XENON

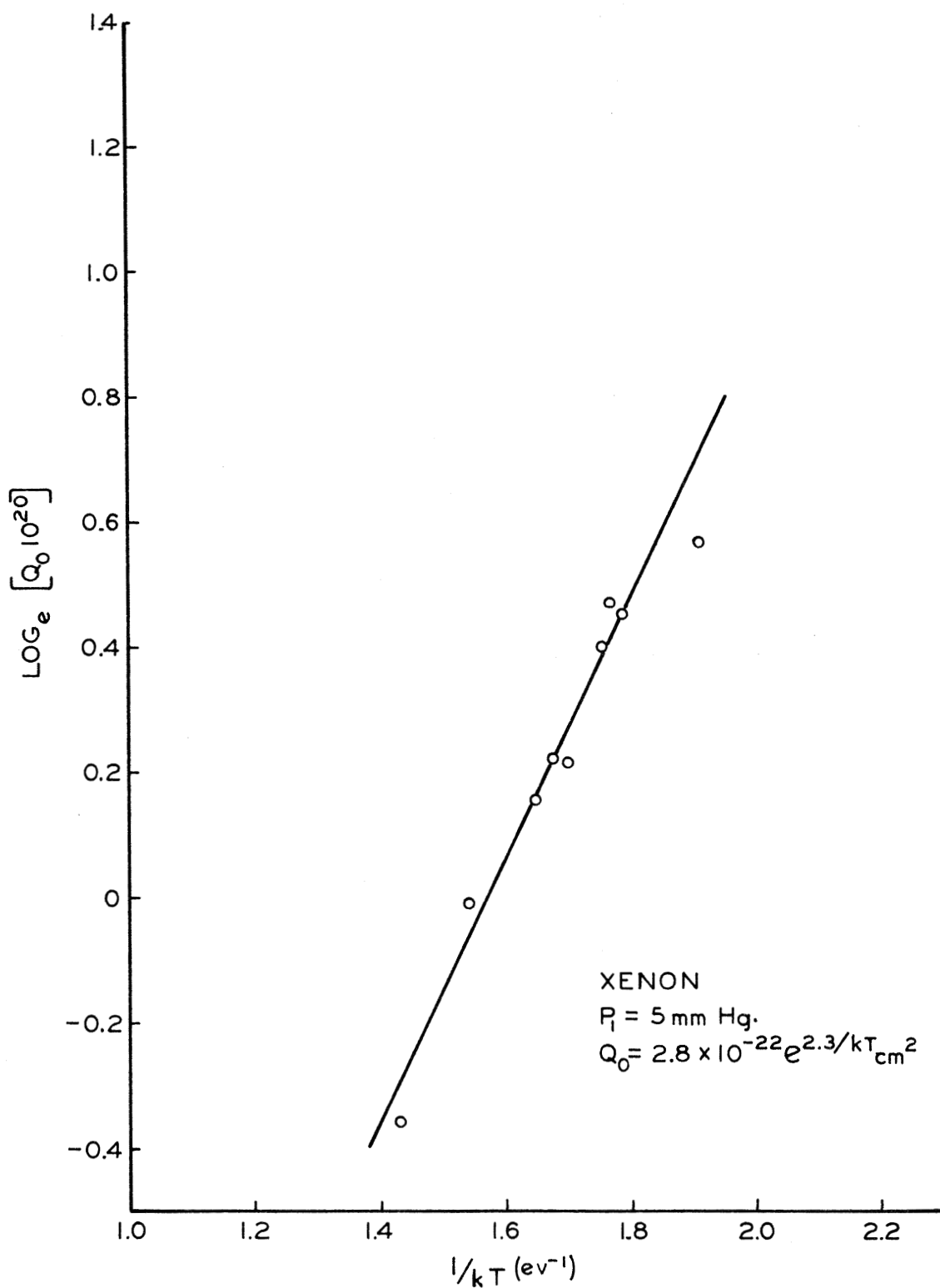


FIGURE 35 CROSS-SECTION DEFINED BY WEYMANN

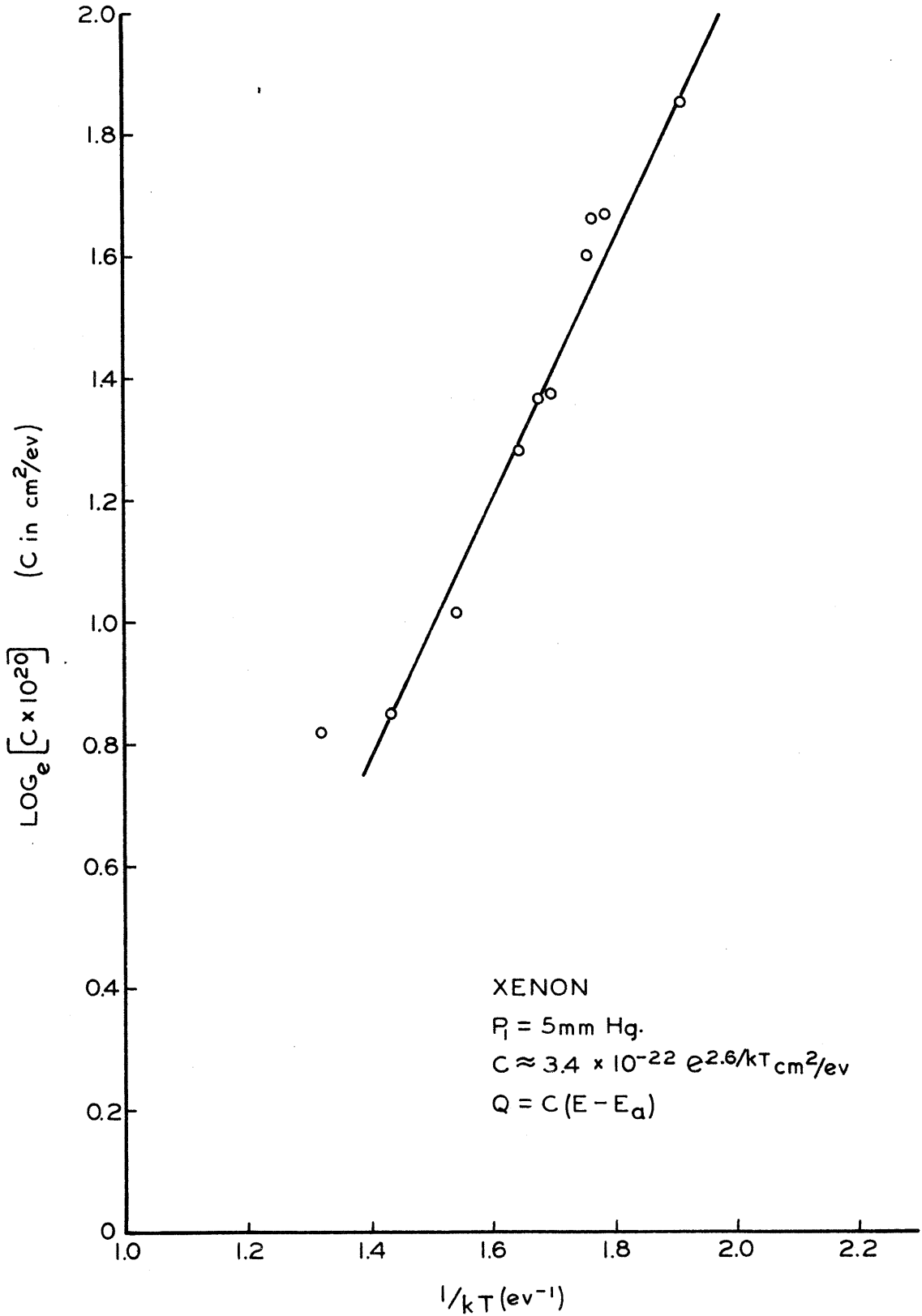


FIGURE 36 CROSS-SECTION PARAMETER C